

Underwater soft-bodied pulsed-jet thrusters: Actuator modeling and performance profiling

The International Journal of
Robotics Research
1–22
© The Author(s) 2016
Reprints and permissions:
sagepub.co.uk/journalsPermissions.nav
DOI: 10.1177/0278364915622569
ijr.sagepub.com



Francesco Giorgio-Serchi^{1,2}, Andrea Arienti² and Cecilia Laschi²

Abstract

A new kind of underwater vehicle is developed by taking inspiration from cephalopods. Its actuation routine is scrutinized via a suitable model. Similar to octopuses and squids, these vehicles consist of an elastic, hollow shell capable of undergoing sequential stages of ingestion and ejection of ambient fluid, which is driven by the recursive inflation and deflation of the shell. The shell actively collapses, and in this way it expels water through a funnel; then it passively returns to the inflated shape, drawing ambient fluid into the cavity. By doing so, a pulsed-jet propulsion routine is performed that enables the vehicle to propel itself in water. Due to their soft nature, the actuation of these vehicles is largely dependent on the subtle management of the elastic response of the shell throughout the propulsion routine. A kinematic model of the actuation mechanism, thoroughly corroborated by experimental validation, is devised which elucidates the relationship between the active (collapse) and passive (refill) stages of the actuation. Upon association with the dynamics of the vehicle, this model permits the derivation of the generic performance profiles of this new kind of vehicle. It is acknowledged that, for given design specifications, an optimal swimming speed exists in coincidence with the coordinated operation between the crank mechanism driving the shell contraction and the onset of elastic energy, which determines the speed of inflation of the shell. These results are invaluable in the definition of rigorous design criteria and derivation of ad-hoc control laws for a new breed of optimized soft-bodied, pulsed-jet, unmanned underwater vehicles.

Keywords

Bioinspired robots, aquatic robots, actuators

1. Introduction

Along with the ever-growing interest for oceanic and marine technologies comes the need to perform construction, maintenance and surveying tasks in ever more challenging scenarios. Autonomous Underwater Vehicles (AUVs) and Remotely Operated Vehicles (ROVs) are being looked upon as an indispensable tool to deal with the increasing spectrum of applications that marine technologies rely on. The former encompass a broad class of sea-dwelling, streamlined vehicles capable of long-distance traveling and suited for data gathering and prolonged surveying across open stretches of water (Singh et al., 1997; Yoerger et al., 2007). These vehicles maneuver via the employment of control-surfaces, which prevent them from performing low-speed and station-keeping/hovering maneuvers. ROVs, on the other hand, comprise box-shaped, thrust-vectoring-endowed vehicles, tethered to the surface for power supply and communication. Thanks to their capability to hover, they represent the workforce in underwater operations where manipulation tasks are required (Choi et al., 2003).

Lately, a concerted effort has been made towards the exploration of novel design criteria, in order to merge the benefit of the autonomous, untethered navigation of AUVs with the fine maneuverability and hovering capability of ROVs (e.g. Yoerger et al. (2007) and Vasilescu et al. (2010)). It is hoped this will tackle the ever-increasing complexity of new underwater scenarios, such as ship-hull inspection (Hover et al., 2012) and marine renewables installation, maintenance and operation (Elvander and Hawkes, 2012). While these contributions are proving invaluable at performing tasks which until recently were infeasible, a concerted effort in the research community has addressed the development of innovative propulsion strategies in order to endow UUVs (Unmanned Underwater Vehicles) with augmented maneuvering skills.

¹Southampton Marine and Maritime Institute, University of Southampton, UK

²Scuola Superiore Sant'Anna, The Biorobotics Institute, Italy

Corresponding author:

Francesco Giorgio-Serchi, Southampton Marine and Maritime Institute, University of Southampton, Southampton, Hampshire, SO16 7QF, UK.
Email: f.giorgio-serchi@soton.ac.uk

By capitalizing on the insight derived from the study of water-dwelling organisms, it is possible to develop a whole new range of bioinspired underwater vehicles which sport highly sought after features in the sector of offshore and underwater operations. From flagellates (Abbott et al., 2009) to turtles (Licht et al., 2004) to octopuses (Sfakiotakis et al., 2014), several aquatic organisms have their own robotic counterpart, covering a broad range of sizes and a variety of locomotion strategies. Certainly, fish-like fin and caudal flapping (e.g. Conte et al. (2010); Saimek and Li (2004); Yu et al. (2004); Zheng et al. (2010)), together with eel-like whole-body undulatory propulsion (Yu et al., 2011) have received greater attention within the research community (Bandyopadhyay, 2005; Colgate and Lynch, 2004).

Newly designed breeds of robotic fish are not only capable of performing fast-start manoeuvres and short-radius turning, but are also being manufactured with highly deformable materials in order to make them resilient to strain and inherently capable of exhibiting continuous body curvature (Marchese et al., 2014). The employment of deformable structures and actuators for developing soft-bodied machines is broadly referred to as soft robotics (Kim et al., 2013; Trimmer, 2013), a fast-paced growing branch of research where robots are composed, to a major extent, of compliant materials capable of withstanding extensive strains whilst exerting limited resistance to compressive and shearing loads.

The strive for developing this new kind of robot has been driven, in part, by the knowledge that issues such as safe physical human-robot interaction and navigation in highly perturbed, unstructured environments can be effectively dealt with by the recourse to soft-bodied robots, rather than by enhancing the complexity of the control (Mörtl et al., 2012; Woodman et al., 2012). The consensus across the research community for this joint soft/bioinspired design approach ultimately resulted in the production of robots that not only benefited from a reduced risk of causing harm or suffering damage, but also that were capable of performing completely new modes of locomotion (e.g. Boxerbaum et al. (2012); Calisti et al. (2011); Lin et al. (2011); Sugiyama and Hirai (2006)), manipulation (Laschi et al., 2009; Xydas and Kao, 1999) and driven by new actuation mechanisms (Cianchetti et al., 2011; Otake et al., 2002; Pelrine et al., 2000).

However, while terrestrial environments pose a significant hindrance to soft-bodied robots (because the lack of a rigid structure forces them to travel by crawling, serpentine or worm-like locomotion), in water this major drawback is overcome. Cephalopoda are the living proof that, in the aquatic environment, the lack of a skeletal supportive structure does not prevent outstanding swimming performances; on the contrary, evidence is emerging that the capability of cephalopods to significantly vary the shape and volume of their body is the key process behind the unsurpassed swimming skills of these organisms (Weymouth and Triantafyllou, 2013). It is

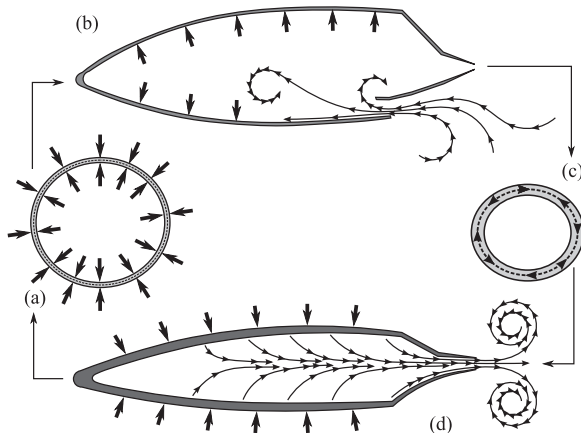


Fig. 1. Schematic depiction of the muscle activation and correspondent inflation-deflation routine in the mantle of a cephalopod performing pulsed-jet propulsion (adapted from Gosline and DeMont (1985) and Anderson and Demont (2000)): (a) the plane view of the radial muscle contraction, which squeezes the cross-sectional thickness of the mantle and drives the expansion of the cavity; (b) the side view of the mantle cavity undergoing inflation and ingesting ambient fluid; (c) the plane view of the circumferential muscle contraction which drives the thickening of the mantle wall and subsequently causes the collapse of the mantle cross-section, and (d) the radial deflation of the mantle with consequent expulsion of the fluid stored within the cavity.

the authors' opinion that, by taking inspiration from cephalopods, it will be possible to design aquatic soft-bodied robots with superior maneuvering ability and highly advantageous structural characteristics.

The aquatic environment and the kind of operations which are performed in proximity to submerged structures is where the assets of an aquatic soft robot could best be put to use. Hence Soft Unmanned Underwater Vehicles (SUUVs) could have an advantage over standard UUVs thanks to their reduced weight, their aptness at complying with complex surroundings, and their intrinsic safety when operating in close synergy with a diver. Pipeline and ship hull inspection, wreck exploration, aquaculture plant survey and underwater archaeology are a few examples where marine operations could profit from the recourse to soft-bodied aquatic machines.

With the exception of Weymouth et al. (2015), the work devoted to cephalopod-inspired locomotion has focused exclusively on implementing the pulsed nature of the propulsion in otherwise standard AUVs. Waterjet propulsion is not new (Allison, 1993) and has been taken into consideration for use in underwater vehicles (Guo et al., 2010; Xin et al., 2013). However, as a variant of the propeller, a waterjet relies on a pump to generate a continuous jet which can be vectored in order to steer the vehicle. In contrast, cephalopod-like pulsed jet propulsion yields increased thrust production (Krueger and Gharib, 2003) and the discontinuous nature of the actuation is regarded as a viable solution for dealing with highly unsteady maneuvering (Krieg and Mohseni, 2008) such as that which

ROVs are exposed to. State of the art cephalopod-inspired vehicles consist of the diaphragm-driven actuator of Krieg and Mohseni (2010), the self-propelled piston-driven Robosquid from Moslemi and Krueger (2010) and that of Ruiz et al. (2011) where a standard propeller linked to a check-valve generates a discontinuous jet by the controlled occlusion of the propeller slipstream. However, external body shape modification and body compliance play a role in enabling cephalopods perform the aggressive unsteady maneuvers sought for in underwater robotics (Weymouth et al., 2015; Weymouth and Triantafyllou, 2013). This either requires the development of new kinds of actuators especially designed for implementation in soft-structured machines, or the adaptation of existing technologies in new mechanical artifacts.

In this paper the design of a new kind of soft-bodied, pulsed-jet thruster previously developed by the authors Giorgio-Serchi et al. (2013b) is reviewed. The performances of three prototypes of this novel type of vehicle are investigated as a means to derive the interplay between actuator kinematics and vehicle dynamics. In particular, the unexpected occurrence of an inverse correlation between pulsation frequency and steady-state speed of the vehicles is analyzed by resorting to a thoroughly validated model of the actuation routine.

The paper is organized as follows: first, the working routine and assets of cephalopod-inspired locomotion are illustrated and then the design concept of a new soft-bodied, pulsed-jet vehicle inspired by these organisms is presented. A series of prototypes based on this design concept and differing in external shape and performances are developed and later tested. The complex dynamics of these vehicles is thus analyzed by devising a suitable model of the actuator which is then validated with ad-hoc experiments. This model is then fed into a whole-body dynamics model of the vehicle. Upon further verification of the reliability of the coupled actuator-vehicle dynamics formulation, the model is eventually employed to perform a conclusive performance profiling analysis.

2. Cephalopod-inspired propulsion

Cephalopods employ species-specific strategies for propelling themselves in water. While squids almost exclusively employ pulsed-jetting (Johnson et al., 1972), cuttlefish are found to rely on finned propulsion, especially in hovering maneuvers. Octopuses, on the other hand, exploit a combination of arm sculling (Kazakidi et al., 2015) and pulsed-jetting. In the present work we will focus exclusively on the last of these modes of aquatic locomotion.

2.1. Cephalopod pulsed-jet propulsion

Pulsed-jet propulsion (Johnson et al., 1972) is a swimming strategy based on a routine of sequential ingestion and expulsion of finite slugs of water from within a cavity of the animal body (Figure 1), the “mantle” chamber, driven by the

inflation (Figure 1(b)) and collapse (Figure 1(d)), of the cavity itself. Inflow of ambient water occurs across ingestion valves, the “pallial valves”, while expulsion is driven across a nozzle, the “siphon”. In Figure 1, siphon shape variations during the pulsed-jetting cycle and additional anatomical features beside the mantle are omitted for clarity; the interested reader is referred to Gosline and DeMont (1985) and Anderson and Demont (2000) for a more rigorous discussion on the role of the distinct anatomical elements throughout the swimming routine.

There are species-specific anatomical differences among the various cephalopods (Gosline and DeMont, 1985), but the basic features entail bundles of longitudinally, radially (as in Figure 1(a)), and circularly (Figure 1(c)) arranged muscles which permit the pressurization and stiffening of the mantle chamber via their concerted contraction; see Thompson and Kier (2006) and Macgillivray et al. (1999) for further reading about muscle structure and activation in squids.

A pulsation cycle can ideally initiate with the refilling of the mantle cavity, guided by the inflation of the mantle chamber due to the antagonistic coactivation of radial muscles versus circular and longitudinal muscles (see Figure 1(a)). The chamber expands, ingesting water across the pallial valves and preventing inflow across the siphon via its collapse, Figure 1(b). At this stage, the fluid expulsion initiates due to the prominent activation of circular muscles over other muscles, Figure 1(c). This causes the diameter of the mantle chamber to decrease, pushing a finite slug of fluid through the siphon, Figure 1(d).

The duration of the entire jetting cycle is species-dependent, varying between about 0.4 s (Anderson and Demont, 2000; Bartol et al., 2009), and 1.0 s (Anderson and Grosenbaugh, 2005) in squids and 1.0 to 1.5 s in octopuses and cuttlefish (Trueman and Packard, 1968). The expulsion phase of the jet varies significantly in duration according to swimming mode, but is found to range between an average value of 0.3 s (Gosline and DeMont, 1985) for squids to 0.6 s (Trueman and Packard, 1968) for octopuses, often constituting about one third of the whole pulsation routine. The pulse-averaged thrust is associated with specimen mass (Trueman and Packard, 1968) and is found to range between 0.02 to 0.05 N in squids with a mean mass of 281 g Anderson and Grosenbaugh (2005); thrust peaks for a 400 g squid lie between 1.0 and 5.0 N, between 0.2 and 0.8 N for a 220 g octopus Trueman and Packard (1968) and between 0.3 and 3.5 N for a 340 g cuttlefish (Trueman and Packard, 1968).

During the cyclic expansion and collapse of the mantle chamber, three major fluid dynamics phenomena participate in making this specific mode of aquatic locomotion especially advantageous.

1. The augmented thrust associated with the pulsed nature of the jet flow that occurs whenever a finite amount of fluid is expelled in a discontinuous fashion from

a converging nozzle (Krieg and Mohseni, 2013). Evidence for this is found in the capability of swimming squids to modulate jet frequency and nozzle shape (Anderson and Grosenbaugh, 2005; Bartol et al., 2009; Staaf et al., 2014), which ultimately affect jet speed and stroke ratio. The amount of thrust produced in this manner is found to be superior to that produced by a comparable continuous jet (Krueger and Gharib, 2003; Ruiz et al., 2011) such as that generated by a common propeller; contrary to what was once believed, it appears to be as efficient as the caudal-flapping propulsion of fish (Staaf et al., 2014).

2. The capability of these soft-bodied organisms for subjecting their body to extensive deformation. Indeed, evidence is emerging that, while accelerating in a dense fluid, the shrinkage of the mantle provides positive feedback on thrust production via the recovery of kinetic energy associated with the variation of added mass (Weymouth et al., 2015; Weymouth and Triantafyllou, 2013).
3. Finally, it can be demonstrated that the boundary layer forming over shrinking bodies participates in impairing the drag by annihilating the separation generated prior to the body shrinkage. Thus it contributes to the reduction of the viscous loads acting against the body during the integral propulsion routine (Weymouth and Triantafyllou, 2012).

The outstanding swimming performances of cephalopods are therefore associated either with the nature of the jet expelled or with the phenomena dependent on the variation of shape which the body undergoes while swimming. Both these aspects are tightly linked to the unique capability of cephalopods to alter their body shape, hence the importance of designing highly deformable vehicles. Designing a fully deformable soft vehicle which performs a swimming routine analogous to that of cephalopods does not only provide an advantage in terms of locomotion performances, but also guarantees resilience to impact and flexibility to move through cluttered spaces or narrow apertures. These characteristics together determine a set of unique assets which no other underwater vehicle possesses.

2.2. Design concept for soft-bodied pulsed-jet propelled underwater vehicles

In order to take advantage of the entire range of assets of cephalopod propulsion, it is necessary to replicate the pulsed-jetting routine by accounting for the actual body-shape changes. In an attempt to design a robotic artifact capable of performing this kind of routine, an effort was made to exploit the overall structural compliance which makes cephalopods unique in the animal kingdom. In this respect, certain design principles pertinent to the emerging field of soft robotics (Trivedi et al., 2008) perfectly lend themselves to the purpose of the present work.

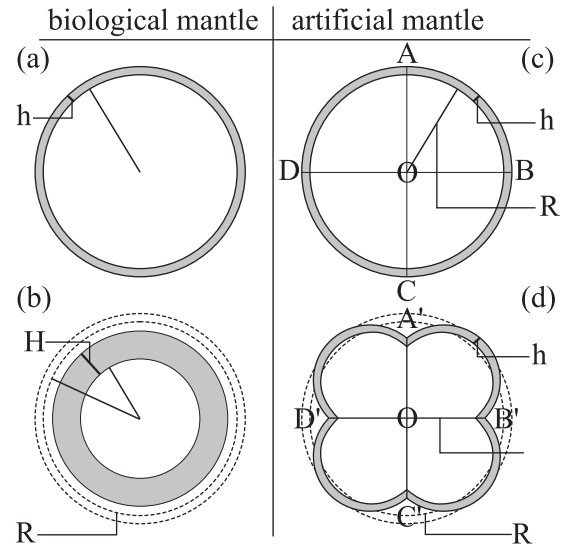


Fig. 2. Schematic comparison between the cross-sectional variation of the mantle of a cephalopod, (a, b) (adapted from Gosline and DeMont (1985)), where cross-sectional thickness varies from h to H , and the robotic counterpart actuated by pointwise cable-driven loading, (c, d). The cables AO , BO , CO and DO are gathered through point O . The number of cables and location of point O are arbitrary, and only four of these are depicted here for the sake of clarity. (a) and (b) show an arbitrary cross-section of the vehicle among those referenced with N in Figure 7.

In our functional surrogate of the cephalopod muscular hydrostat (Thompson and Kier, 2006), the robotic artefact essentially consists of a hollow shell of rubber-like material which acts like the mantle of a cephalopod. This elastic chamber hosts the purposely designed mechanical parts which drive the collapse. The inflation, and hence the refill of the chamber, is non-controlled and spontaneously driven by the resilient nature of the silicone: the underactuated degree of freedom is thus dealt with by the elasticity of the shell. Cable transmission associated with an electric motor was designated as the most convenient actuation system because of its efficiency and because it warrants a remarkable design flexibility, as shown in Figure 2.

The actual working routine entails a sequence of cyclic phases of collapse and inflation of the elastic chamber. The compression stage of this elastic chamber is executed by the shortening of a series of cables fitted, at one end, to the elastic walls of the mantle (points A, B, C and D in Figure 2(c)) and, at the other end, to a crank (Figures 4 and 7), the rotation of which cyclically pulls and releases the cables. The inward displacement of the attachment points gives rise to a lobe-shaped deformation of the walls of the shell (Figure 2(d)), which in turn pressurizes the internal fluid, accelerating it through a nozzle located at one end of the elastic shell. In order for the elastic chamber to be collapsed as homogeneously as possible, the cables must be evenly pulled radially inward at the same time and by the same extent, regardless of their attachment point over the

shell. This is enabled by resorting to a kind of fixed pulley (point O in Figure 2(c) and (d)) through which the cables are gathered. This pointwise loading of the shell, which drives the buckling of the silicone structure in the proximity of the cable fittings, distinguishes the artificial mantle from its biological counterpart (compare Figure 2(b) with (d)).

The refill phase, i.e. the ingestion of ambient fluid, occurs passively by exploiting the elastic potential energy charged in the shell during the cable-driven collapse. Upon replenishment of the elastic chamber, a new pulsation can take place.

2.3. Prototype manufacturing

Three prototypes (previously reported by Giorgio-Serchi et al. (2013a,b,c) are employed here for the purpose of analyzing both the working routine of the actuator and the whole-body dynamics of the vehicles. These models have been reviewed below for the reader's convenience. Upon acknowledgement that fast pulsation frequencies are detrimental to thrust production for such vehicles (Giorgio-Serchi et al., 2013a), design improvements consisted of the enhancement of expelled volume per pulsation and the decrease of actuation frequency (Giorgio-Serchi et al., 2013c). This is enabled by increasing the stiffness of the shell (as in Prototype-2, below) and by increasing the number of sections of the mantle which are collapsed, along with the employment of a motor suited for operating at lower rpm (as in Prototype-3).

1. Prototype-1, Figure 3(a), consists of a mould of Ecoflex 00-30TMsilicone cast into an ellipsoid of revolution. The actuation of Prototype-1 is driven by 6 equally distributed nylon cables attached over one single cross-section of the elastic shell via the actuator depicted in Figure 4(a). A crescent-shaped ingestion valve located underneath the nozzle helps support the refill stage. The robot is 160 mm long from the foremost to the rearmost point, 95 mm wide and 80 mm tall at the largest cross-section. The whole prototype, including electronics and mechanical components, weighs 333.5 g, of which 212.0 g is silicone. The rigid components thus represent only 36.5% of the mass of the whole robot. The maximum expellable amount of fluid per pulsation is 59 mL, equivalent to 17% of the volume contained within the shell prior to shrinkage. Tests are performed with two gearmotors, a GM11A and a GM11A Solarbotics, in order to span a range of operation between 0.5 and 6.5 pulsations per second (pps).
2. Prototype-2, Figure 3(b), consists of a thick-walled shell molded into a torpedo-like shape; similar to Prototype-1, the actuation mechanism is guided by four nylon cables distributed over a single cross-section of the shell. As in Prototype-1, inflow during the refill stage of the vehicle occurs through a crescent-shaped

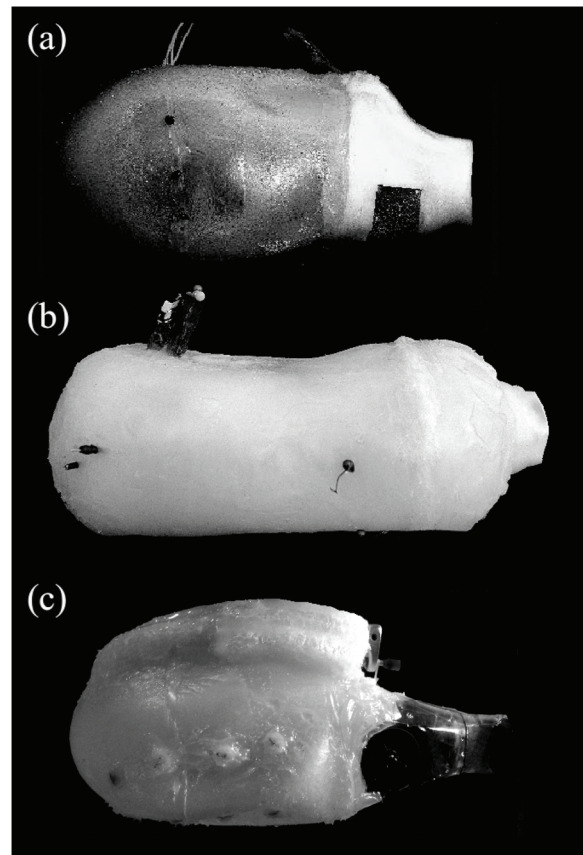


Fig. 3. The three prototypes of the soft-bodied pulsed-jet thruster developed by the authors: (a) Prototype-1 (Giorgio-Serchi et al., 2013b), (b) Prototype-2 (Giorelli et al., 2013; Giorgio-Serchi et al., 2013a) and (c) Prototype-3 (Arienti et al., 2013; Giorgio-Serchi et al., 2013c).

curtain-like valve. In its final stage, the robot is 210 mm long from the foremost to the rearmost tip, has a 40 mm internal radius and weighs 550 g. Rigid components amount to a mere 3% of the whole mass of the vehicle which is capable of expelling as much as 100 mL of the total 527 mL (representing the internal volume at the initial stage). The motor, a GM12A Solarbotics, enables the actuator to run within the range of 0.73 to 2.6 pps.

3. Prototype-3, Figure 3(c), was molded from the same cast as Prototype-1, but the shrinkage of this artificial mantle is executed throughout the whole axial extent of the shell by placing five nylon cable attachment points at four sections along the axis of the shell, see the actuator outline in Figure 4(b). This grants Prototype-3 with the capability to expel as much as 120 mL of the internal fluid, i.e. approximately 34% of the initial volume. The refill stage of the vehicle is dealt with by the recourse to three umbrella valves located around the base of the nozzle. The motor chosen, a Maxon 320177 DC Motor, allows the vehicle to pulse within the 0.88 to 1.5 pps range.

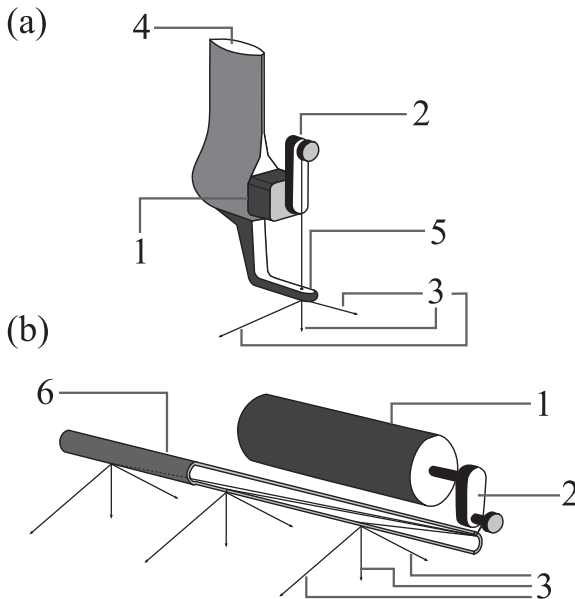


Fig. 4. Schematic depiction of the actuator employed in Prototype-1 and 2 (a) and Prototype-3 (b). Numbers refer to: [1] the motor, [2] the crank, [3] the cables, [4] the point of anchorage between actuator and the shell, [5] the fixed pulley, [6] the axial fixed pulley.

2.4. Prototype testing

In order to assess the pulsed-jetting routine of the vehicles, tests were performed in a controlled environment and evaluated in terms of the kinematics of the translational speed of the prototypes. The experiments were performed in a 1150 mm long, 590 mm wide and 500 mm deep tank filled with tap water. The vehicles were allowed to travel along a straight line inside the tank by letting the motor revolve at a quasi-constant angular velocity. The tests consisted of recording the displacement of the vehicles as they travel from one end of the tank to the other. Due to the prototypes not being neutrally buoyant, a hull-shaped foam float was employed to maintain them at a steady height below the free surface and to help them to travel along a straight line during experimentation (by sliding along a wire fitted to the distal sides of the tank). No apparent disturbances associated with the experimental rig were observed, with the exception of the abrupt vehicle slowdown as it approached the end wall of the tank. Recorded data were taken into consideration only prior to the occurrence of such an effect. The tests were recorded with a digital camera at 25 fps and subsequently treated with image tracking software and a Savitzky-Golay low-pass filter to process the displacement and velocity temporal profiles.

A qualitative comparison between the performances of the three vehicles is portrayed in Figure 5, and a comparison of average speed values is reported in Figure 6. The vehicles were subjected to a sequence of repetitive tests performed at progressively increasing pulsation frequencies. By comparing the average swimming speeds of

the vehicles, it appears that higher frequencies of pulsation do not necessarily lead to higher swimming speed, see Figure 6. The complex dynamics involved in the activation of the soft robots is apparent in this set of results, where Prototype-3 undergoes a completely different pattern from Prototype-1 and Prototype-2. Whilst the latter manifests a clear inverse correlation between pulsation frequency and average swimming speed, the former behaves in the opposite way.

In order to explain these trends, the interplay between the actuator and the elastic shell of the vehicle must be taken into consideration. A major factor in determining the performance of the soft-bodied thrusters is represented by the mechanism of passive inflation of the mantle chamber. The stresses within the elastic wall of the mantle give rise to the expansion of the chamber which, in turn, drives the ingestion of ambient water. Because this mechanism is passive, the recharge time is fixed and is solely determined by the geometry and constituent materials of the shell. This suggests that, in order for the thruster to perform a functional cycle of pulsation, the speed of revolution of the crank driving the shell collapse has to be slow enough for the mantle walls to inflate and, in this way, refill the chamber. In this respect, it is reasonable to expect that a fast sequence of pulsation causes the inflation of the mantle to become less effective at refilling the mantle cavity, which causes an impoverished capability of the routine to generate thrust (provided that the increased speed of ejection does not compensate for the depletion of ejected mass). This trend is apparent in the tests performed with Prototype-1 and Prototype-2, while the tests performed with Prototype-3 highlight a reversed trend. This analysis does not consider a series of additional terms which take part in the thrusting routine, such as the dynamic effect associated with the nature of the pulsed jet (Krieg and Mohseni, 2013) and the recovery of added mass due to the collapse of the shell (Weymouth and Triantafyllou, 2013).

The examination of the divergent results manifested by the prototypes provides us with an insight into the thrust characterization of this underactuated, flexible body-dependent routine. Each profile of pulsation frequency vs. average speed can be thought of as a function with the shape of a log-normal distribution, where the maximum coincides with the point when the crank angular velocity and the speed of inflation of the elastic shell are perfectly synchronized. When this condition is met, the refill time is exactly coincident with the time it takes the motor to cover half a revolution.

Ahead of this peak, performances are expected to improve at increasing pulsation frequency, while beyond the peak they worsen, because the shell does not have enough time to inflate and the motor runs idle for a brief time, during which thrust is not generated. According to this interpretation, the data from Prototype-3 lie in the increasing performance branch of their respective profile, while the tests from Prototype-2 lie in the decreasing performance

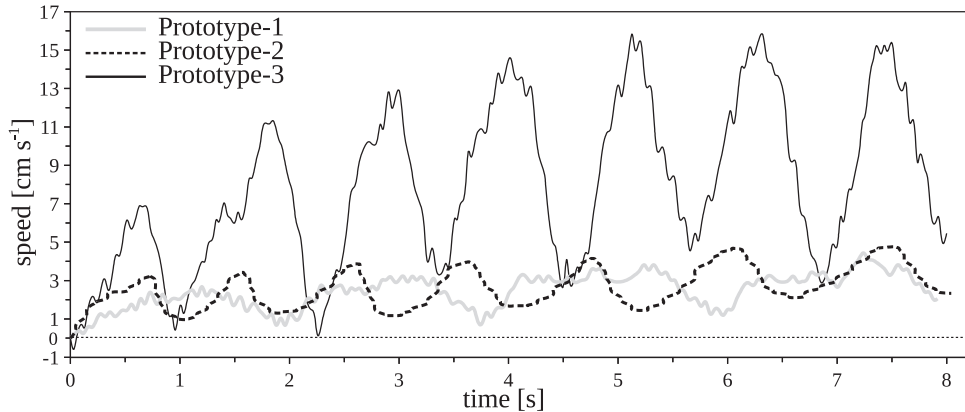


Fig. 5. Velocity profiles from tests performed at the lowest operational pulsation frequency allowed by motor specification of the three SUUVs shown in Figure 3: 0.5 pps for Prototype-1, 0.73 pps for Prototype-2 and 0.88 pps for Prototype-3.

side of their own trend. If confirmed, this hypothesis provides us with useful information as to the optimal design parameters and working routine of the actuator. Hence, the need arises to devise a tool which may provide a clarification on the hypothesis made and eventually aid in the estimation of the performances of new prototypes.

3. Actuator modeling and validation

Based on the comparison of the three prototypes (Figure 6), evidence emerges that the passive response of the shell to the actuation routine plays a crucial role in determining the performances of this new kind of vehicle. This gives rise to the fairly complex problem of hydroelasticity (Giorgio-Serchi et al., 2015) which goes beyond the scope of the present work. In what follows, we focus on describing the simplest model conceivable to account for the pulsed-jet thrust production routine without neglecting the buckling-like effect of each cable-driven actuation and the passive inflation of the shell. Given the generic geometrical features of the actuator (see Figure 7) and the various mechanical components which enable the actuation of the vehicle (Figure 4) and its propelling routine in water, it was possible to derive a set of equations which permit the characterization of the thrust production routine and, in turn, the vehicle performance in water.

This model enables prediction of the thrust produced by the process of expelling finite slugs of fluids via the pointwise collapse of an elastic shell. The thrust is derived by accounting for the instantaneous variation of the area of a cross-section of the shell being collapsed (by the traction of cables attached over its internal walls). First, it is shown how the area within a cross-section of the elastic shell subject to pointwise cable-driven collapse is computed. This is later related to the whole volume expelled by the thruster at each pulsation. Eventually, this will be fed into a one-dimensional dynamic model of a rigid body translating in water in order to predict the actual locomotion performance of the vehicle.

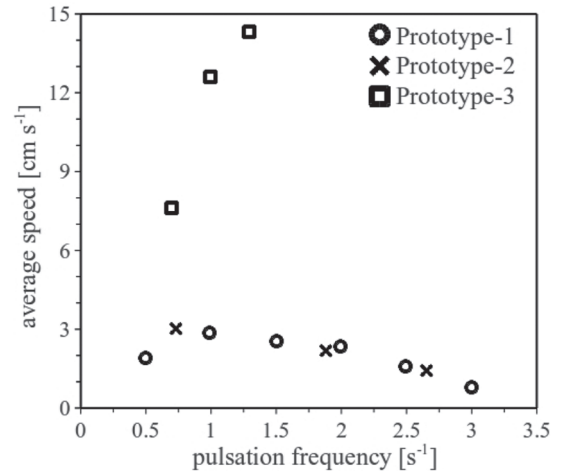


Fig. 6. Profiles of the averaged speed of the vehicle versus frequency of pulsations.

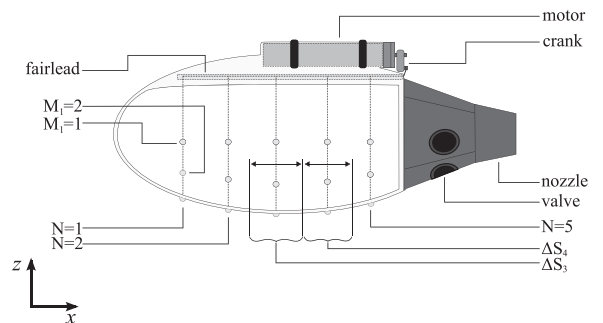


Fig. 7. Schematic of the constitutive elements of the soft-bodied thruster. N refers to the cross-sections where cables are attached along the vehicle axis; M_N are the spots, over each cross-section N , where cables are attached; ΔS_N is the axial extent by which the pointwise loading of the cables affects the shell.

The vehicle translates along the sway direction x , thus having its cross-section lying on the yz -plane, see Figures 7 and 8. The vehicle consists of a hollow shell of length L made of a rubber-like material, see Figure 3. The shell is

divided into N cross-sections, each of which is located at a distance $\Delta S_N/2 + \Delta S_{N+1}/2$ from the other, see Figure 7. The term ΔS_N thus represents the axial extent of a slice of shell centered at the axial location of the cross-section N , which is affected by the traction of the cables acting over that cross-section.

At each cross-section, M cables are attached along the circular perimeter of the shell, at angles γ_{NM} with respect to the center C of the cross-section (and origin of the reference frame), as depicted in Figure 8(a), where the subscripts correspond to the section and the cable indices, respectively. At each of the N cross-sections, the M_N cables are attached, at one end, to the wall of the rubber shell and, at the other end, are gathered through a fixed pulley located in vertex O at γ_O . This guides the cables to a crank, the rotation of which sequentially pulls and releases the cables, see Figure 4. The crank is of length l and revolves at an angular speed ω . The frontal area of the vehicle is equivalent to a semi-sphere with radius R_1 , analogous to that of the first cross-section $N = 1$, where R_N is the radius of cross-section N in its unstrained state. The two end points of the arc of circumference (which delimit the silicone body in which the fairlead is immersed) remain unaffected by the cable-driven collapse. In the case depicted in Figures 8(a) and (b), these are located at A_{N4} and A_{N5} , placed at angles γ_{N4} and γ_{N5} with respect to C . Hence, over each cross-section, there are $K_N = M_N + 2$ geometrical vertices ($A_{N1}, A_{N2}, \dots, A_{NK}$), two of which are fixed (i.e. A_{N4} and A_{N5} in the case of Figure 8(a)).

The shortening of the cables occurs due to the crank rotation, which, by pulling the M_N points distributed over the shell cross-section N , deforms the shell into a lobe-shaped geometry with $i_N = K_N - 1$ lobes, as depicted in Figure 8(b). The model employed here approximates these newly generated lobes to arcs of circumferences and assumes that the arc length between two cable-affected spots is conserved during deformation. Given a certain cable contraction c , the M_N points over each cross-section undergo a displacement along the direction of the cable equivalent to ε , see Figure 8(b). Notice that ε can differ from c because of the amount of stretch of the shell material during cable traction, and because of the speed of inflation of the shell during cable release, as illustrated in the following. The displacement of the cable attachment points is related to the cross-sectional area variation using simple geometrical arguments, which are illustrated in Figure 8(b) and explained below.

Let us consider a generic cross-section N of the shell illustrated in Figure 8(b). The cables run through the fixed pulley, vertex O in Figure 8(b), and are linked to the $K = 1, 2, 3, 6$ spots (vertices $A_{N1}, A_{N2}, A_{N3}, A_{N6}$ in Figure 8(b)). Because all the cables are gathered through the fixed pulley in O , once the crank starts revolving around the shaft, they all get pulled the same length ε , as depicted in Figure 8(b). The location of O is arbitrary and dictated essentially by design specifications: for instance in Prototype-1 (Figure 3(a)), the use of the actuator depicted in

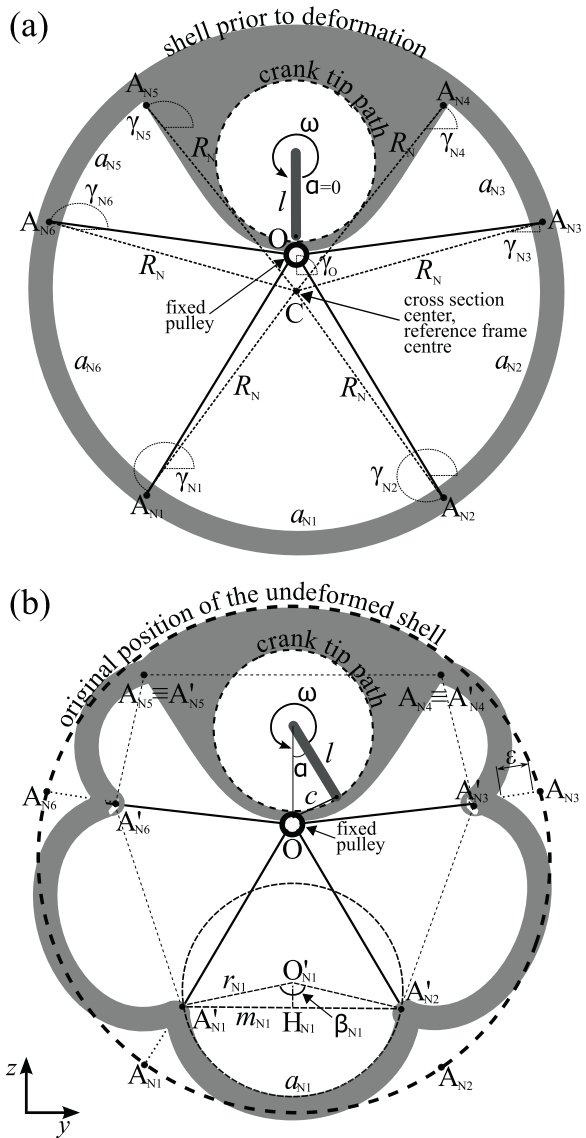


Fig. 8. Schematic depiction of a generic cross-section of the shell acted upon by inward pulling cables: (a) prior to deformation, and (b) after deformation.

Figure 4(a) requires the fixed pulley to be located at coordinates $(0, -1.2)$, see Table 1. On the other hand, Prototype-3 (Figure 3(c)) relies on the actuator of Figure 4(b) (see also Figure 7), thus having $O(0, 3.6)$, see Table 3.

Given the extent of the cable shortening by the crank and the coordinates of the vertices in the unstrained state A_{NK} , the new position of these vertices in the collapsed configuration, A'_{NK} , is computed by translating such vertices along the direction of their respective cables. For those spots which are not subject to cable-driven collapse $A_{NK} \equiv A'_{NK}$, as in points A_{N4} and A_{N5} in Figure 8(b), the shortening of the cables deforms the shell into a lobe-shaped geometry with i_N lobes, as depicted in Figure 8(b). Let us consider lobe $i_N = 1$ in Figure 8(b); here points A_{N1} and A_{N2} of Figure 8(a) are displaced to their new positions A'_{N1} and

A'_{N2} . By approximating the lobes to arcs of circumference, the reduction of the cross-sectional area can be computed in terms of the change from the initial circular sector $A_{N1}\widehat{O}A_{N2}$ (Figure 8(a)) to $A'_{N1}\widehat{O}A'_{N2}$ (Figure 8(b)).

To do so, the time-varying parameters $a_{N1}(t)$, $m_{N1}(t)$, $r_{N1}(t)$ and $\beta_{N1}(t)$ are defined respective to the arc, the chord, the radius and the angle subtended by the arc $a_{N1}(t)$ at time t . For the reader's convenience, time dependence is omitted in the reminder of the discussion. Of all these, only a_{N1} and the respective coordinate positions of A'_{N1} and A'_{N2} (and therefore m_{N1}) are known. Given a_{N1} and m_{N1} , it is possible to compute the area of the circular sector $A'_{N1}\widehat{O}A'_{N2}$ by noting that

$$\frac{\overline{H_{N1}A'_{N1}}}{\overline{O'_{N1}A'_{N1}}} = \frac{m_{N1}}{2r_{N1}} = \sin \frac{\beta_{N1}}{2} \quad (1)$$

where O'_{N1} is the center of circle of radius r_{N1} . Since $r_{N1} = a_{N1}/\beta_{N1}$ of the circular segment, then

$$\frac{m_{N1}}{2a_{N1}}\beta_{N1} - \sin \frac{\beta_{N1}}{2} = 0 \quad (2)$$

The solution to this non-linear equation outputs a value for β_{N1} , and therefore r_{N1} . This allows us to compute the area \mathbb{A}_{N1} of the circular segment comprised between m_{N1} and a_{N1} , by subtracting the triangular area of the triangle $A'_{N1}\widehat{O}_{N1}A'_{N2}$ from that of the circular sector $A'_{N1}\widehat{O}_{N1}A'_{N2}$

$$\mathbb{A}_{N1} = \frac{1}{2}r_{N1}a_{N1} - r_{N1}\cos\left(\frac{\beta_{N1}}{2}\right)\frac{m_{N1}}{2} \quad (3)$$

By repeating this operation over each lobe i , then subtracting the area of the triangle determined by the fixed pulley and the fixed spots (i.e. circular sector $A'_{N4}\widehat{O}A'_{N5}$ in Figure 8(b)) and adding the area of the internal polygon delimited by the A'_{NK} vertices, the cross-sectional area \mathbb{A}_N associated with the contraction c , at time t , is obtained

$$\begin{aligned} \mathbb{A}_N = & \sum_{i=1}^{K-1} \left[\frac{1}{2}r_i a_i - r_i \cos\left(\frac{\beta_i}{2}\right) \frac{m_i}{2} \right] - \mathbb{A}_{FP} \\ & + \frac{1}{2} \left[\sum_{h=1}^{K-2} y_{A'_{Nh}} z_{A'_{Nh+1}} + y_{A'_{NK-1}} z_{A'_{N1}} \right. \\ & \left. - \sum_{h=1}^{K-2} y_{A'_{Nh+1}} z_{A'_{Nh}} - y_{A'_{N1}} z_{A'_{NK-1}} \right] \end{aligned} \quad (4)$$

Here, the second term on the right hand side (RHS) of equation (4), \mathbb{A}_{FP} , refers to the part of the cross-sectional area which does not undergo deformation, and the geometrical specifications of which are prescribed by design. For the case depicted in Figure 8, for instance, $\mathbb{A}_{FP} = A'_{N4}\widehat{O}A'_{N5} = A'_{N4}\widehat{C}A'_{N5} - A'_{N4}\widehat{C}A'_{N5} + A'_{N4}\widehat{O}A'_{N5}$.

The third term in equation (4) is Gauss' formula for the area of the internal polygon defined by A'_{NK} vertices, where $(y_{A'_{NK}}, z_{A'_{NK}})$ are the coordinates of a generic vertex A'_{NK} , which vary according to

$$y_{A'_{NK}} = y_{A_{NK}} - \varepsilon(t) \cdot \cos(\gamma_{NK})$$

$$z_{A'_{NK}} = z_{A_{NK}} - \varepsilon(t) \cdot \sin(\gamma_{NK})$$

Hence, given the angle spanned by the crank, it is possible to achieve an estimate of the change in area of a certain cross-section of the shell via equation (4). It is thus possible to estimate the amount of instantaneous ejected mass of fluid by relating the variation of \mathbb{A}_N with ΔS_N , that is, the extent in the axial direction of the region subject to deformation, see Figure 7. Hence, the expelled amount of mass of fluid is equivalent to

$$\begin{aligned} \frac{dm}{dt} = & \rho \frac{dV}{dt} = \rho \sum_{k=1}^N \Delta S_k \frac{d\mathbb{A}_k}{dt} = \\ = & \rho \left[\Delta S_1 \frac{d\mathbb{A}_1}{dt} + \Delta S_2 \frac{d\mathbb{A}_2}{dt} + \dots + \Delta S_N \frac{d\mathbb{A}_N}{dt} \right] \end{aligned} \quad (5)$$

Because the shell undergoes an actuated, cable-guided phase and a non-actuated, resilience phase, the term $d\mathbb{A}_N/dt$ cannot merely be computed by relating the variation of the cross-sectional area to the angular rotation of the crank. In the experiments presented in earlier work (Giorgio-Serchi et al., 2013b, 2015), the interplay between motor rotation and the resilience of the shell was shown to be a key element in determining the dynamics of the robot. A simple formulation for such interaction is devised as follows with reference to Figure 9.

Given a constant angular velocity of the motor, the time-varying extent by which the crank pulls the cables is described by

$$c = 2l \sin \frac{\alpha}{2} \quad (6)$$

where

$$\alpha = \int \omega dt \quad (7)$$

being $0 < \alpha < 2\pi$. Because the rubber material undergoes a certain degree of stretch during cable contraction that depends on the thickness of the shell wall and the Poisson module of the material, the actual arc length may be slightly longer after deformation. This effect is accounted for in the present model by introducing a coefficient of stretchability C_s . Hence, $\varepsilon = C_s c$, C_s provides an estimate of the extent by which the rubber material becomes stretched and permits us to empirically match the model results with the experimental observations.

Beside the degree of stretch of the hyperelastic material, the displacement ε of a point on the shell acted upon by a cable (such as A_{N1} in Figure 8(b)) may differ from c because of the mismatch between the crank angular velocity and the speed of shell inflation. A solution to equation (6) is depicted in Figure 9(a). Each rotation of the crank draws a trough-like profile of the displacement of the cable attachment point. In Figure 9, the shell is initially in an unstrained state and then starts to be collapsed, see the section of the profile with $\frac{d\mathbb{A}_N}{dt} < 0$. The deepest point of the trough corresponds to the maximum contraction, beyond which the crank starts to release the cables and the shell

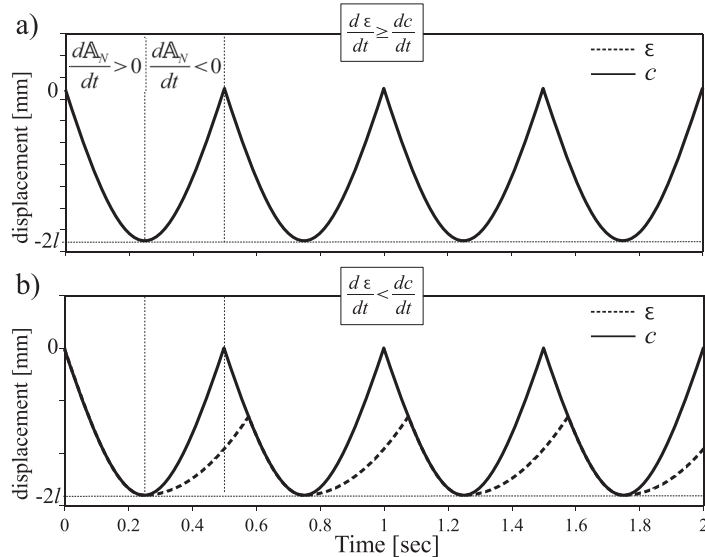


Fig. 9. Temporal profile of the displacement ε of a cable attachment point along the cable direction (i.e. point A_{N1} along $\overline{A_{N1}O}$ in Figure 8) in the special case when $C_s = 1$ and $\omega = 6.28$ rad/s: in (a), the case with $\frac{d\varepsilon}{dt} \geq \frac{dc}{dt}$, where the shell inflates as fast or faster than the release of the cables and, (b), the case with $\frac{d\varepsilon}{dt} < \frac{dc}{dt}$, where the inflation time of the shell is slower than the release of the cables by the crank.

inflates, $\frac{d\mathbb{A}_N}{dt} > 0$. The peak in the profile corresponds to the unstrained state of the shell. The case depicted in Figure 9(a) represents the condition in which the point on the shell moves synchronously with the crank during both contraction and release of the cable (i.e. $\varepsilon \equiv c$), hence the profiles overlap. This may occur when the process of inflation of the shell is as fast or faster than the cable release. Because the shell walls and the crank are linked, the limiting speed in this case is that of the crank. In these cases, the displacement of a point of attachment of the cables over the shell follows exactly the profile generated by the rotation of the crank, see Figure 9(a).

However, at fast revolution of the crank, the speed of inflation of the shell can be lower than the speed of cable release. This occurs when the time it takes the shell to return to its unstrained state is longer than the time it takes the crank to cover the second half-rotation. In this case, when the crank has completed one full rotation, the cables are still loose because the shell is still in the process of inflating (i.e. $\varepsilon \neq c$). The contraction can start over only when the cables tighten, which occurs at the point of intersection between the profile drawn by the crank and that drawn by the shell (Figure 9(b)). The resilience of the shell is described here by a simple quadratic function in which a coefficient V_e determines how fast the shell inflates. This behavior is formulated as follows

$$\frac{d\mathbb{A}_N}{dt} < 0 \Rightarrow \varepsilon \equiv c = 2C_s l \sin\left(\frac{1}{2} \int C_\tau \omega dt\right), \quad (8a)$$

$$\left\{ \begin{array}{l} \frac{d\mathbb{A}_N}{dt} > 0, \\ \end{array} \right. \left\{ \begin{array}{l} \frac{d\varepsilon}{dt} \geq \frac{dc}{dt} \Rightarrow \varepsilon \equiv c = 2C_s l \sin\left(\frac{1}{2} \int \omega dt\right), \\ \frac{d\varepsilon}{dt} < \frac{dc}{dt} \Rightarrow c \neq \varepsilon = 2 \int V_e dt, \end{array} \right. \quad (8b)$$

where V_e is determined empirically by accounting for the time it takes the shell to fully re-inflate and C_τ accounts for the drop in angular velocity of the motor while loaded with a resistive torque. The relationship expressed by equations (8a)-(8c) accounts for the fact that, during contraction, $\frac{d\mathbb{A}_N}{dt} < 0$, the shell deforms at the speed of loaded crank rotation (equation (8a)); during inflation, $\frac{d\mathbb{A}_N}{dt} > 0$, the shell either follows the unloaded crank speed rotation, (equation (8b)) or an arbitrary quadratic function (equation (8c)), depending on whether passive inflation or crank rotation is quicker.

By accounting for the interaction between the process of cable-driven collapse and the inflation of the shell, a realistic description of the temporal evolution of ε is achieved. This in turn is employed to derive the displacement of the cable attachment point along the direction of its respective cable and, in this way, obtain the new configuration of the shell cross-section (from A_{NM} to A'_{NM}). Once implemented in Octave (Eaton, 2002), this enables us to compute the value of \mathbb{A}_N at consecutive instants and from this compute $\frac{d\mathbb{A}_N}{dt}$ to solve equation (5), which is essential for estimating the thrust production routine.

3.1. Experimental apparatus

The actuator model is verified by comparing it with a purposely-designed experimental set-up which enables quantification of cross-sectional variation of a cylindrical shell acted upon by inward pointwise loads. This experimental rig consists of a cylinder of rubber-like material perforated at equally distributed spots over a single cross-section placed at half its height. Inextensible cables are fitted to the silicone wall of the cylindrical shell and gathered

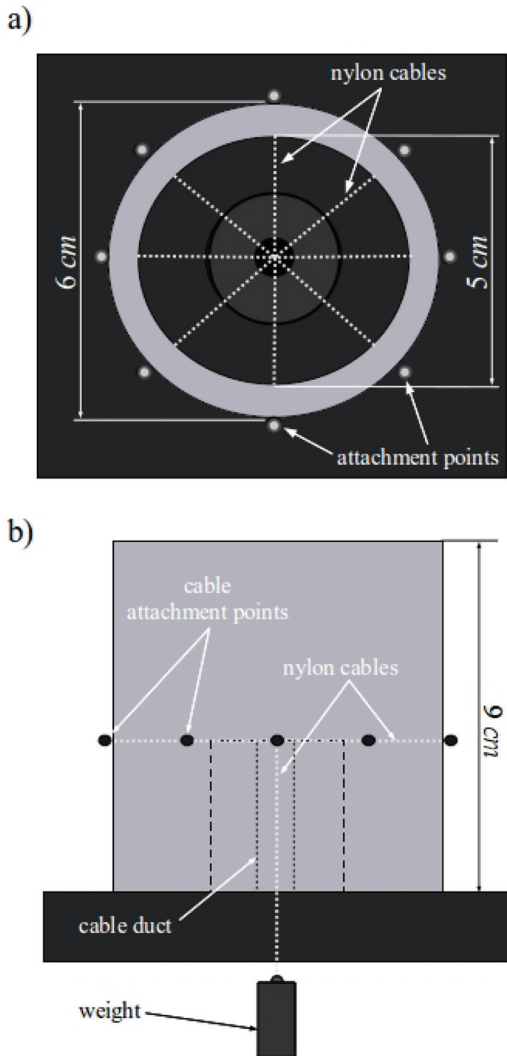


Fig. 10. Plane view (a) and lateral view (b) of the experimental rig for measuring cross-sectional change of the elastic shell during cable-driven deformation.

radially at the center of the cylinder through a cable-duct, see Figure 10(a) and (b). This cable-duct is a cylindrical conduit which collects the cables in a single spot concentric to the external silicone cylinder, acting as point O in Figures 2 and 8, i.e. the fixed pulley. The silicone cylinder and the cable-duct are fastened to a platform attached to a rigid frame in order to allow the cables, which run across the cable duct, to hang freely below it. By hanging loads to the bundle of cables the cross-sectional deformation of the silicone shell is achieved (Figure 10(b)).

In the present case a 90 mm long cylinder of ECOFLEXTM00-30 silicone is molded. The cylinder has a 25 mm internal radius and a 5 mm thick wall. The cylinder is pierced at ten equally spaced spots along a single cross-section at its mid-length. Ten nylon dyneema cables are passed through the points of perforation of the shell. The cables can be pulled separately or as a single bundle. This simplified experimental rig provides us with a means

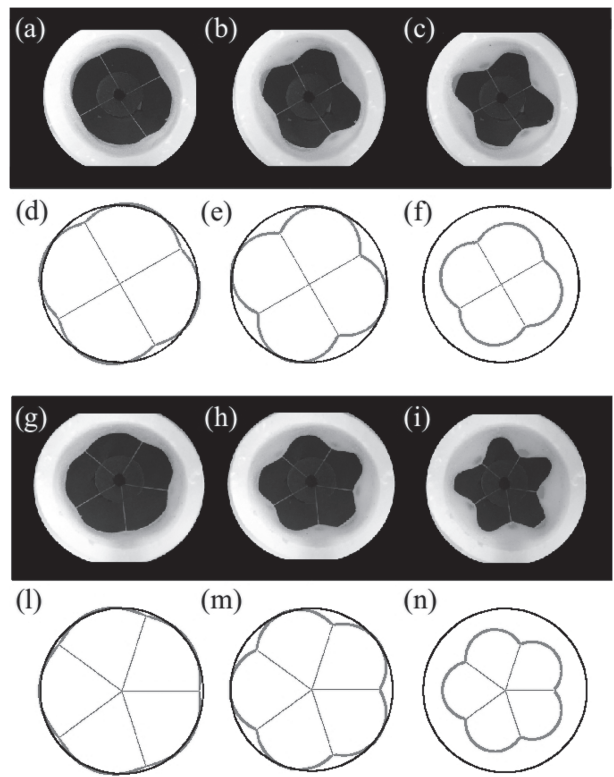


Fig. 11. Qualitative representation of the cross-sectional area evolution at successive stages of cable shortening: pictures are taken at 0.5 cm, 1.0 cm and 1.5 cm cable shortening. Comparison between the experimental (a, b, c) and simulated (d, e, f) 4 cable test and the experimental (g, h, i) and simulated (l, m, n) 5 cable test.

to quantitatively estimate both the cross-sectional change at the plane acted upon by the cables and the force required to do so. Force measurements are inferred from the weights suspended at the free end of the cable bundle. Cross sectional variations are measured by digitally thresholding the frames taken during the experiment at successive stages of loading. After thresholding, an area detection is performed which eventually leads to an image of the strained cross-section of the cylinder at the plane acted upon by the cables. This, upon calibration with the known length scale of the rig frame and integration, allows calculation of the instantaneous area within the shell walls.

The experiment is performed by hanging a load of given weight to the bundle of cables, allowing the elastic walls to attain a static equilibrium and then measuring the extent which the cables have been pulled radially inward, followed by the digital treatment of the cross-sectional area. Because the structural characteristic of a silicone cylinder is easily affected by the casting procedure and the process of polymerization, potentially leading to non-negligible discrepancies between tests, three identical cylinders are employed for the same test and each measurement is repeated three

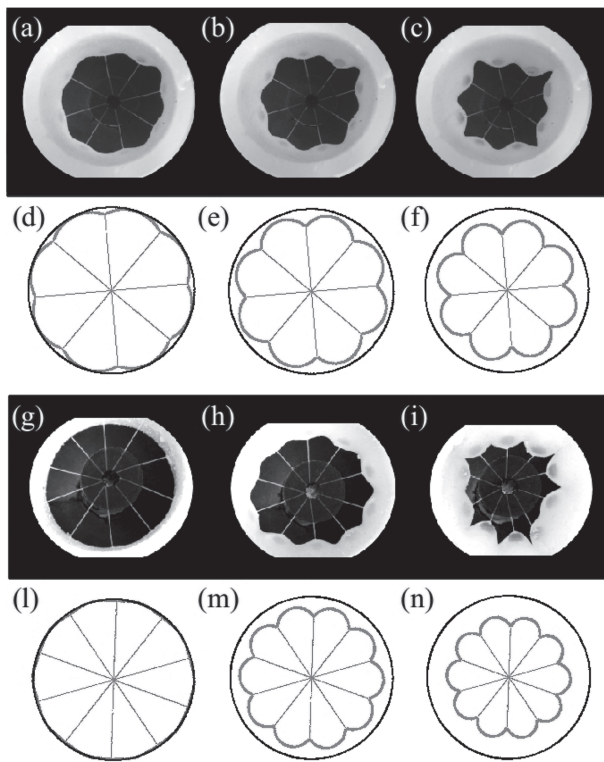


Fig. 12. Qualitative representation of the cross-sectional area evolution at successive stages of cable shortening: pictures are taken at 0.5 cm, 1.0 cm and 1.5 cm cable shortening. Comparison between the experimental (a, b, c) and simulated (d, e, f) 8 cable test and the experimental (h, i, l) and simulated (m, n, o) 10 cable test.

times. Reported data are achieved by performing an ensemble averaging over the three repeated measurements across the three cylinders.

3.2. Kinematics model validation

Four sets of tests are performed, with 4, 5, 8 and 10 cables evenly distributed over the mid-height cross-section of the silicone cylinder (presented in Figure 10) and evenly pulled from the center of the cylinder. The cables are subject to progressively increased loading in order to associate cable shortening with cross-sectional variation. The model of equation (4), upon suitable calibration of the C_s coefficient of equation (8a), is used to simulate these series of tests. The results of the qualitative comparison between the model and the experiment are shown in a series of snapshots taken at three successive conditions of cable shortening (i.e. at 50 mm, 100 mm and 150 mm) in Figures 11 and 12. Quantitative comparison of the experimental and simulated values of cross-sectional area variation as a result of cable shortening is reported in Figure 13.

The model employed here becomes dramatically less accurate at predicting the internal area as both the number of cables and loading are increased, see the comparison

between Figure 12(c) and (i) with (f) and (n). This is consistent with the measurements of cross-sectional variation becoming less accurate at increased loading; in particular, in the case where a higher number of cables is employed (see Figure 13(d)), due to the increased stiffness of the rubber-like material associated with increased tangential strain. Decrease in model accuracy is in part due to imperfections in the experimental rig and in the silicone cast used, which contribute to a loss of axial symmetry in association with increased strain. On the other hand, the major limitation of the present model lies in the impossibility of describing the cross-sectional deformation of the silicone walls as they depart from the idealized circular-shaped lobe geometry. In order to account for these internal strains and shears, full three-dimensional structural models are needed. However, the model employed performs well within the degree of deformation which the vehicles being considered go through during their operative cycle.

These results also bring evidence that, while the employment of a higher number of cables does provide a more homogeneous collapse of the shell, the increased load required to collapse them is not substantiated by a proportional increase of squeezed area. This justifies the recourse, in the design of the actual prototypes, to a lower number of cables.

These tests represent an idealized vehicle design, where the cable traction occurs from the center of the shell and acts at evenly distributed spots over the shell. The actual design of the vehicles employed here differs from this configuration in that parts of the shell are excluded from the action of the cables and that cable contraction does not necessarily occur through a spot placed in the center of the shell. However, these tests have demonstrated that the kinematics model can satisfactorily capture the buckling-like cross-sectional collapse of the elastic shell for cable shortening of up to 40% of its radius. The area variation computed in this way can thus be reliably employed for the estimation of the water volume ejected from the vehicle. This term is central to the description of the thrust production routine and, eventually, to the estimation of the whole-body dynamics of the vehicles in water.

4. Prototype dynamics modeling and validation

A model can be formulated to predict the performances of the vehicles of Figure 3 by employing a standard one-dimensional momentum equation for a rigidly translating, neutrally buoyant body traveling in water along the sway direction. This is formulated as follows

$$M \frac{dU}{dt} = -\frac{1}{2} \rho C_d \mathbb{A}_{ref} U |U| - X_{AM} \frac{dU}{dt} + \tau \quad (9)$$

where U is the x component of velocity of the robot and M is the overall mass of the robot comprising silicone, mechanical/electrical parts and the time-varying mass of

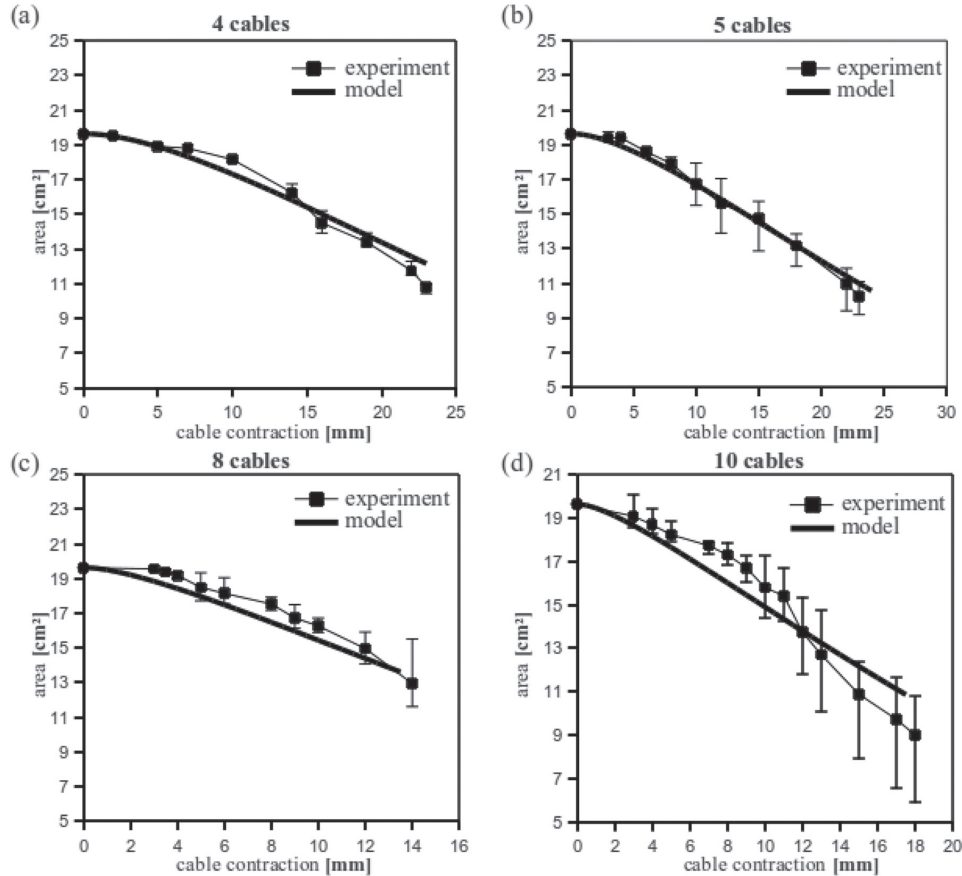


Fig. 13. Quantitative comparison of cable contraction versus cross-sectional area variation in the 4, 5, 8 and 10 cable configuration between the experimental and simulated cases. Experimental data are reported as ensemble averaging and maximum data deviation over three repeated measurements over three analogous cylinders.

water stored in the elastic chamber. The RHS term represents the drag, with C_d being the drag coefficient, \mathbb{A}_{ref} a reference area of the body and ρ the fluid density; the second RHS term is the added mass, with X_{AM} being the axial added mass coefficient, and $\tau = q \cdot dm/dt$ the thrust term. The thrust is defined in terms of the speed outflow q across the nozzle-exit area \mathbb{A}_{nz} , while the expression for dm/dt is provided in equation (5). The speed of the issuing fluid across the nozzle is given by

$$q = C_f \frac{1}{\rho \mathbb{A}_{nz}} \frac{dm}{dt} \quad (10)$$

where C_f defines a flow loss coefficient at the nozzle-exit plane which depends on the direction of the flow

$$\left\{ \begin{array}{l} \frac{dm}{dt} > 0 \Rightarrow C_f = C_{f1} \leq 1.0 \\ \frac{dm}{dt} < 0 \Rightarrow C_f = C_{f2} < 1.0 \end{array} \right. \quad (11a)$$

$$(11b)$$

The choice for the appropriate value of C_f is based on the amount of fluid flowing across the nozzle alone. This parameter serves the purpose of accounting for the fact that, during expulsion, the flow must converge across the nozzle in order to maximize thrust; during the refill phase of

the vehicle, inflow across the nozzle should be restricted in order to minimize backward thrust and ease inflow through valves oriented normal to the traveling direction.

This was attempted, in the vehicle, via the incorporation of passive curtain (Prototype-1 and 2) and umbrella (Prototype-3) valves which are sealed during jet expulsion and opened during the refill stage. This differs from the mechanism adopted by cephalopods, where the inflow through the siphon during inflation is prevented via its collapse, and leaking through the pallial valves is impeded during jet expulsion via their sealing (Staaf et al., 2014).

According to Prandtl (1952), the coefficient of contraction of the flow at a thin-walled circular opening and the occurrence of ingestion valves which partially prevent the inflow during inflation from taking place across the nozzle can be estimated (see Figure 14). The outflow and inflow loss coefficients are taken to be $C_{f1}=0.85$ and $C_{f2}=0.6$.

By substituting equation (5) in equation (10) above, the following is achieved

$$q = \rho \frac{C_f}{\mathbb{A}_{nz}} \left(\sum_{k=1}^N \Delta S_k \frac{d\mathbb{A}_k}{dt} \right) \quad (12)$$

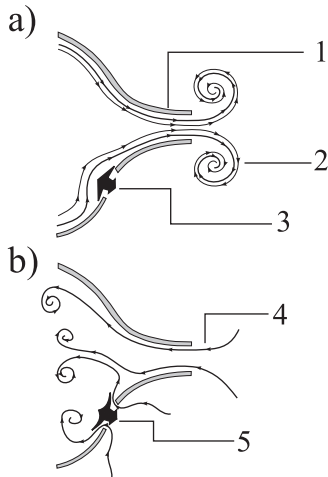


Fig. 14. Schematic visualization of (a) the expulsion and (b) ingestion flow across the nozzle and valves. Numbers refer to: (1) the nozzle, (2) issuing vortex ring, (3) sealed umbrella check valve during outflow, (4) inflow during suction and (5) open umbrella check-valve.

which provides us with the following expression for the thrust

$$\tau = \frac{C_f}{A_{nz}} \left(\rho \sum_{k=1}^N \Delta S_k \frac{dA_k}{dt} \right)^2 \quad (13)$$

The remaining terms in equation (9) are addressed below, with reference to the generic design of the vehicles (see Figure 7). All the elements can either be computed theoretically or measured directly from the assembled robotic platform and specific values for each term are reported in Tables 1, 2 and 3, for Prototype-1, 2 and 3, respectively.

Hence, $M = M_{th} + m$, where M_{th} is the inertia of the thruster. In the case of Prototype-3, this inertia depends on a hollow ellipsoid with the revolution of rubber material (of density ρ_{rb} , radius r_{th} , length l_{th} and thickness t_{th}) which contains mechanical and electrical parts (including one DC motor and the crank mechanism), where m is the time-varying amount of water stored within the shell.

The term X_{AM} is the added inertia of the thruster, approximated, in this case, to an ellipsoid of revolution with minor axis equal to $2R_1$ and major axis L , where $A_{ref} C_d$ is the product of the reference area of the thruster $A_{th} = \pi R_1^2$ and the drag coefficient of a rough-surface short cylinder C_{dth} .

After writing the derivatives as centred differences, equation (9) can be integrated.

4.1. Vehicle dynamics verification

The model is employed for simulating the performances of Prototype-1, 2 and 3, with reference to the design specifications and the hydrodynamic parameters listed in Tables 1 to 3 (reported in the Appendix). This entails, first, simulating the pattern of deformation of these vehicles and, estimating the thrust production routine according to the formulation

described by equations (4) and (13). As an example, the results from the kinematic modeling of the shell deformation under cable pointwise loading are shown in Figure 15 for the case of Prototype-3. Prototype-3 is taken as the case study because it better highlights the capability of the model to capture less symmetrical design features. Prototype-3 hosts the crank mechanism outside the shell, and cable pulling is executed via an axially oriented annular fixed pulley located along the dorsal part of the vehicle, as in Figure 7, which distributes the contraction over four cross-sections of the shell.

A qualitative depiction of the evolution of one of the four cross-sections of the shell acted upon by the cables is reported in Figure 15. Here, the stages of progressive deformations are reported for cable shortenings ranging from 0.2 to 2.0 cm. Figure 15 shows how the model accounts for the parts of the shell, filled gray, which are excluded from the deformation (these are the areas of the vehicle where mechanical and electrical components are stored).

Quantitative estimation of area shrinkage at the four cross-sections is reported in Figure 16, where the comparison between the actual configuration of Prototype-3 and the ideal case with 5 evenly distributed cables pulled from the center of the shell is depicted. Mismatch at zero contraction between the ideal and actual case is due to the occurrence, in the latter, of parts of the shell which do not undergo deformation, i.e. the gray parts within the shell of Figure 15. Upon integration of the cross-sectional shrinkage along the axial direction, the maximum ejected volume within a single pulsation is estimated at 130 mL, which closely compares with the value measured from the actual vehicle.

From the simulation of Prototype-3, actuated with a constant motor crank rotation $\omega = 7.65$ rad/s, we also report the temporal profiles of thrust, nozzle volume outflow, nozzle speed outflow, drag and added mass in Figure 17. The translational speed for this test is depicted in Figure 20(b). Figure 17 provides an insight in the mechanics of Prototype-3: Figure 17(a) shows that, because of suction across the nozzle, the thrust acts both forward and backward, respectively, during expulsion (i.e. descending segment of the volume outflow profile) and ingestion (i.e. ascending segment of the volume outflow profile) of ambient fluid. However the impulse computed over the expulsion is higher than that during ingestion, eventually providing a positive forward acceleration. This is because the outflow takes place exclusively across the nozzle, while the inflow occurs only partially across the nozzle (see Figure 14), branching through the ingestion valves which minimize the negative contribution of thrust. This is further supported by the difference in flow speed across the nozzle during outflow and inflow, see Figure 17(b), motivated by a slower speed of inflation of the shell as opposed to the higher speed of collapse due to cable shortening.

One further remark concerns the role played by added mass in this highly non-stationary mode of propulsion, see

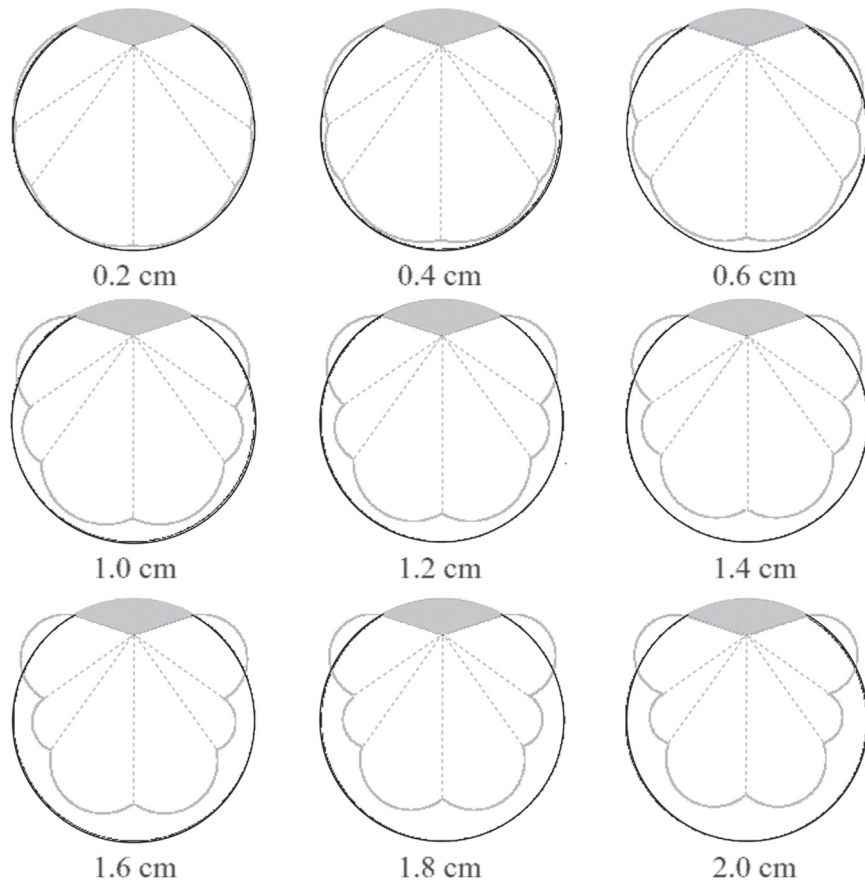


Fig. 15. Simulated cross-sectional variation for Prototype-3 resulting from cable shortening from 2 mm to 20 mm. Cables are dashed gray lines, silicone parts are colored gray and the initial unstrained location of the shell is colored black.

Figure 17(c). The added mass acts against the positive forward acceleration of the vehicle during the expulsion stage of the pulsation (i.e. the added mass has the same sign as the drag in Figure 17(c)) and acts against deceleration during the non-propulsive stage of the pulsation (i.e. the added mass has the opposite sign to the drag). In the present formulation the coefficient of added mass is taken to be constant and hence the resistive force due to added mass varies solely according to the acceleration of the vehicle. As a matter of fact, the shape change which occurs during the collapse/inflation cycle of the vehicle should account for the variation of the added mass coefficient. As postulated in Weymouth and Triantafyllou (2013), the decrease of added mass during collapse of the shell can be adjusted to provide a positive feedback on thrust. This was further reinforced by experimental evidence in Weymouth et al. (2015). In addition, active control upon the increase of added mass during inflation of the shell could be exploited to counteract the deceleration of the vehicle. As far as the present work is concerned, it is not possible to ascertain the occurrence of any measurable added mass variation-induced effect on thrust in Prototype-1, 2 and 3. While more advanced experiments are needed to prove that the specific design of the soft-bodied pulsed-jet thrusters adopted here is, indeed,

apt for exploitation of the added-mass variation effect, the observations presented suggest the existence of interesting ways to enhance the performance of these vehicles solely by tweaking the relative speed of the collapse/inflation stages.

The validity of the model is assessed by comparing the simulated and recorded axial speed of the three prototypes, Figure 3. The results are shown in Figures 18 to 20 for Prototype-1, 2 and 3, respectively. For each prototype, two experiments performed at different pulsation frequencies are considered. In each of the tests examined, the vehicle initially has an unstrained shell; the actuator is then switched on and the vehicle is observed during its translation from one end of the experimental tank to the other. A good match is observed between the modeled and experimental data, especially for the low-frequency cases (Figures 18(a), 19(a) and 20(a)). The discrepancy between simulations and measurements occurs, in certain cases, at the initial stages of acceleration, during which the motor approaches a quasi-steady angular velocity (see the first 7 seconds of Figure 19(a) and the first 3 seconds of Figure 20(b)). The more peaked profiles of the experimental tests might be due to an overestimate of the added mass coefficient in the model or to the effect associated with the occurrence of pitching moments of the actual vehicle

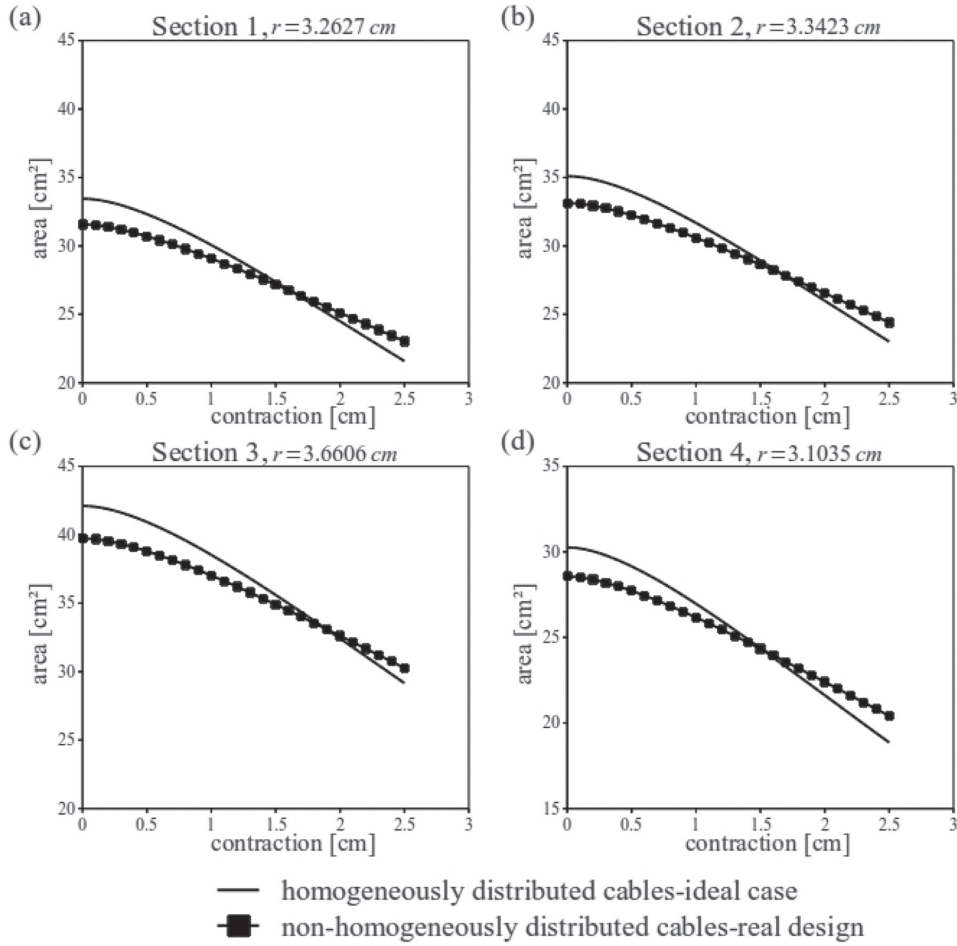


Fig. 16. Area variation due to cable contraction for Prototype-3 at the cross-sections located at four locations along the vehicle axis. In each subfigure, the comparison between the case of a cross-section acted upon by 5 evenly distributed cables and the same cross-section acted upon by 5 cables distributed as in Figure 15, i.e. in the actual case of Prototype-3, is portrayed.

(which the model neglects) which become especially pronounced at high pulsation frequencies, as in Figures 18(b) and 19(b).

4.2. Vehicle performance profiling

The results presented in Figures 18 to 20 show the capability of the model in describing the 1D dynamics of the new kind of pulsed-jet underwater vehicles presented in this work. At this stage the model is further employed to expand the data derived from the profile curves of Figure 6. While the actual prototypes are restricted to an operational regime within a certain, fairly limited, range of pulsation frequencies (due to motor specifications), the model can be used to perform vehicle performance predictions which account for a broader range of frequencies. This is used here to corroborate the hypothesis according to which performances of the vehicles can be estimated, which is, to a large extent, based on the coordination between the crank revolution and the inflation time of the shell.

To do so, we resort to the modeling setups for Prototype-1, 2 and 3 (see Tables 1 to 3 of the Appendix), already employed for the simulations depicted in Figures 18 to 20, and reiterate a 25 second long simulation for each prototype with a 0.075 pps increment. This yields forty 25 second long simulations of each prototype, actuated at pulsation frequencies which range from 0.125 to 3.125 pps. The axial speed predicted by each of these 120 simulations is averaged over the simulation duration and plotted in Figure 21, along with the experimental mean values of Figure 6.

According to the hypothesis, the effect of pulsation frequency on average speed in soft-bodied pulsed-jet vehicles should draw a profile characterized by a maximum of average speed, coincident with the case of synchronous operation of the actuator rotation (i.e. the shell collapse) and the shell inflation. This hypothesis is fully supported by the results achieved via the simulations presented in Figure 21.

The profiles of vehicle performances predicted by the model confirm the existence of a distinct trend in which the performances can be found to improve or worsen according

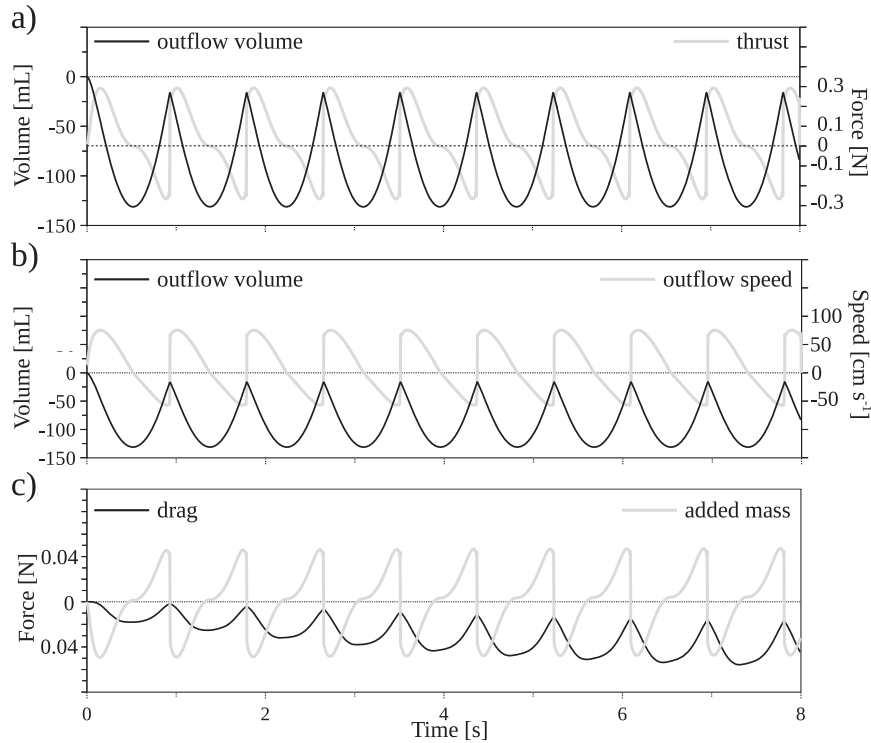


Fig. 17. Simulated temporal profiles of various parameters pertaining to the test depicted in Figure 20(b) for Prototype-3: (a) volume outflow across the nozzle, black, and thrust, gray, (b) volume outflow, black, and speed of the flow at the nozzle, gray, (c) drag, black, and added mass, gray.

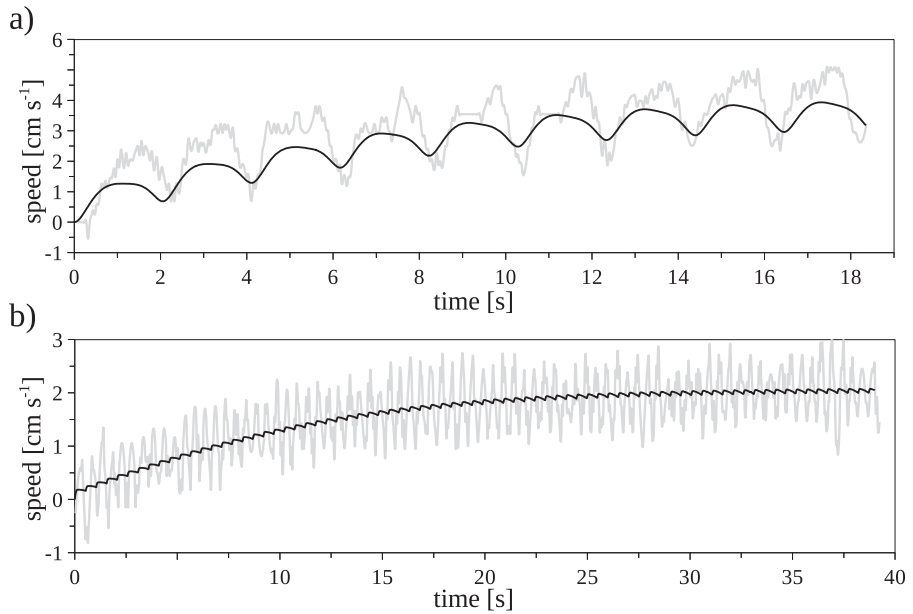


Fig. 18. Simulated (black) and experimental (gray) performances of translational velocity of Prototype-1 at (a) 0.5 and (b) 2.0 pulsations per second.

to whether the cable shortening speed is slower or faster than shell inflation. When the two match, a maximum in average speed is encountered and the vehicle operates at its optimum. The simulations also confirm that Prototype-3 was operating in the increasing performance range of its

own profile, while Prototype-1 and 2 were both in their decreasing performance segment.

The simulations also highlight the occurrence of a minimum in the average speed profile, which arises at very low pulsation frequency (when the expulsion phase is so slow

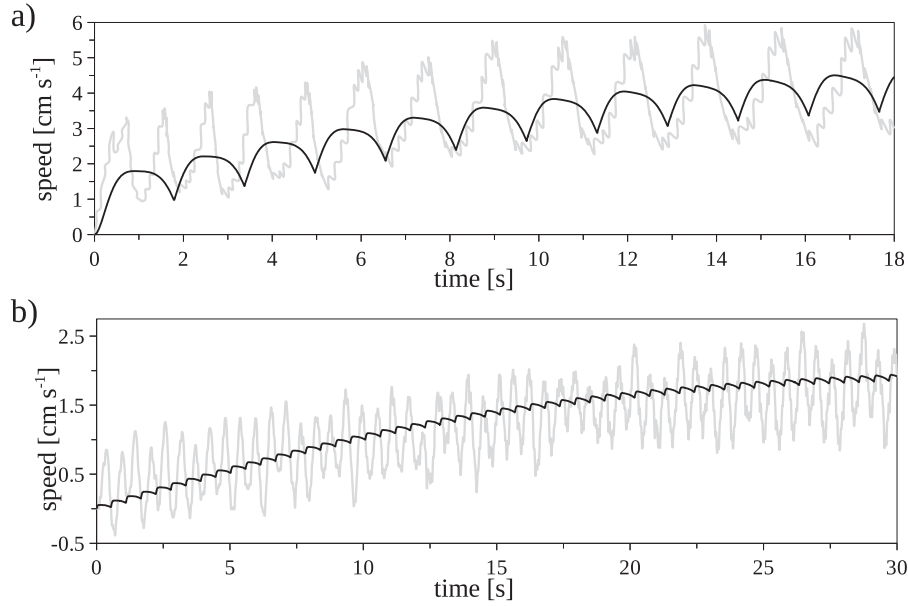


Fig. 19. Simulated (black) and experimental (gray) performances of translational velocity of Prototype-2 at (a) 0.73 and (b) 1.77 pulsations per second.

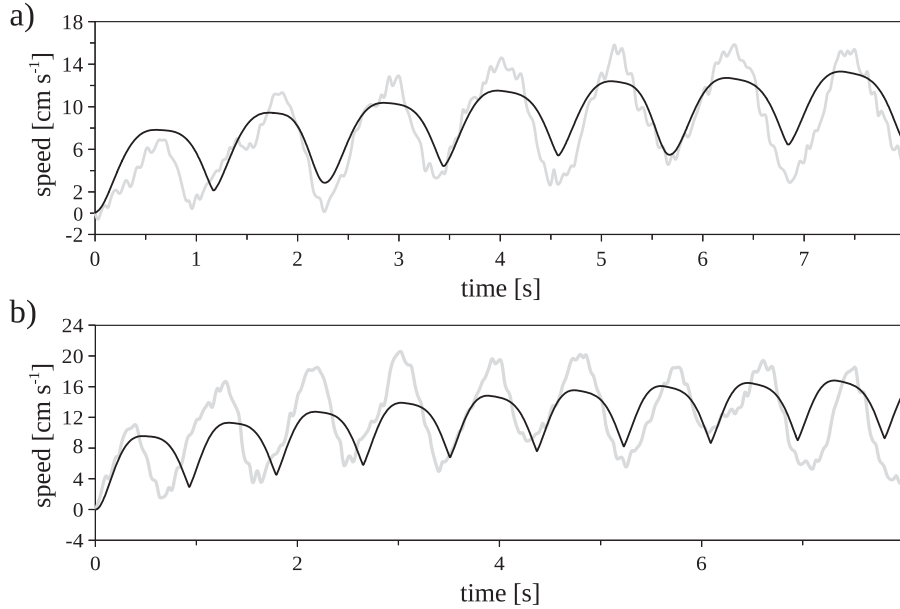


Fig. 20. Simulated (black) and experimental (gray) performances of translational velocity of Prototype-3 at (a) 0.88 and (b) 1.13 pulsations per second.

that the contribution from the suction of fluid during shell inflation is overwhelming), thus providing a net negative thrust to the vehicle.

These results are of importance to the study of this new kind of vehicle because they provide a general characterization of a generic soft-bodied pulsed-jet thruster. The acknowledgement that the interplay between the active and passive phase is a major factor in the thrust production routine provides us with a rationale for evaluating optimal design parameters and actuation routines. Indeed, upon rigorous treatment of the entire actuation dynamics via the

inclusion of both mechanical and material characterization of the actuator, new SUUVs can be developed which operate consistently in proximity of the peak of maximum performance.

5. Conclusion

We have developed an innovative kind of underwater robot inspired by cephalopods, in order to exploit the advantages provided by the swimming strategy these aquatic animals

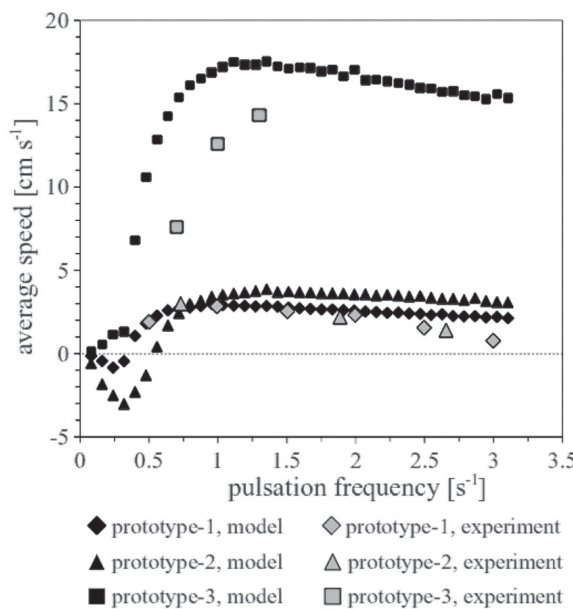


Fig. 21. Modeled and experimental vehicle performances at different pulsation frequencies. Mean speeds are achieved, in simulation, from a 25 s interval averaging. Mean speeds from experiments are achieved from time averaging over the experiment duration.

employ. Cephalopods are peculiar in that they thrust themselves in water by means of pulsed-jetting, a methodology of thrust generation driven by sequences of abrupt inflation and collapse of a soft, collapsible chamber. Other than for their superior locomotor skills, our interest has been drawn to cephalopods due to their unconventional structural characteristics: lacking, for the most part, a proper skeletal system, these organisms are an ideal source of inspiration for the design of soft-bodied vehicles. Superior maneuverability and enhanced structural compliance are highly sought after features in underwater robotics. This has motivated our desire to develop a trustworthy new class of underwater soft robots resemblant of cephalopods.

A series of prototypes was developed which potentially accounted for the whole range of benefits provided by cephalopod-inspired locomotion, i.e. the pulsed nature of the jet, the recovery of added mass due to body-shape changes and the structural compliance of the system. We complement the design of these new vehicles with a model which, despite its simplifications, provides us with a means to investigate the highly non-linear interactions which arise from the non-stationary actuation routine, the resilient nature of the vehicle and its dynamics in a quiescent fluid. Upon validation, this model is extensively exploited concurrently with experimental tests, with the scope of elucidating a generally valid performance profile distinctive of such vehicles.

The analysis corroborates the hypothesis according to which, for given design specifications (crank length, size,

geometry and material properties of the elastic shell, number and arrangement of the cables employed), an optimal swimming speed exists in coincidence with the synchronous action of the actuator (which operates the shell collapse) and the development of elastic energy (which determines the speed of inflation of the shell). Ahead of this maximum, the time taken by shell to inflate is shorter than that taken by the crank to cover its second half rotation: this causes the cables to lie loose for an interval during which thrust is not generated. In this case, increasing the crank angular velocity reduces the time gap during which thrust is not generated, thereby raising the vehicle performance. Beyond the maximum, the time it takes the crank to cover its second half rotation is shorter than that which requires the shell to refill. Thus, when the crank has completed a full revolution and it could ideally start a new contraction, the cables are still loose. This causes the motor to run idle until the cables are tightened again, during which time thrust has not been generated. Despite an increase in crank rotation positively affecting the speed of the issuing jet, the combined effect of increased speed of the outflow with the decreased mass outflow results in a progressively declining performance. At this stage, vehicle output speed can only be improved by reducing the crank angular velocity.

These results are insightful for the design criteria that will require consideration in the development of the next soft-bodied pulsed-jet vehicles, emphasizing the importance of the geometrical/material properties of the shell responsible for the refill phase of the pulsation. This relies on adequate characterization of the elastic components of these vehicles (Renda et al., 2015a,b,c), in combination with a rigorous treatment of the fluid flow occurring both at the nozzle-exit-plane and around the shape-changing vehicle, in order to infer the extent by which these contributions, upon suitable tweaking, can provide positive feedback to the vehicle performances.

The pursuit of this interesting problem of hydroelasticity, partly substantiated by the results presented here, discloses fascinating lines of research at the interface between robotics and hydrodynamics and provides an insight into the technological development of this new breed of aquatic vehicles.

Funding

This work was supported by the European Reintegration Grant funded project CFD-OctoProp [project reference 269477 of the FP7-PEOPLE scheme]; the Foundation Grant of the Fondazione Livorno within the project PoseiDRONE.

References

- Abbott JA, Peyer KE, Cosentino Lagomarsino M et al. (2009) How should microrobots swim? *The International Journal of Robotics Research* 28: 1434–1447.

- Allison J (1993) Marine waterjet propulsion. *NAME Transactions* 01: 275–335.
- Anderson EJ and Demont ME (2000) The mechanics of locomotion in the squid *Loligo pealei*: Locomotory function and unsteady hydrodynamics of the jet and intramantle pressure. *Journal of Experimental Biology* 203: 2851–2863.
- Anderson EJ and Grosenbaugh MA (2005) Jet flow in steadily swimming adult squid. *Journal of Experimental Biology* 208: 1125–1146.
- Arienti A, Calisti M, Giorgio-Serchi F et al. (2013) Poseidrone: Design of a soft-bodied rov with crawling, swimming and manipulation ability. In: *MTS-IEEE OCEANS*, San Diego, CA, USA, 23–27 September 2013, pp. 1–5.
- Bandyopadhyay PR (2005) Trends in biorobotic autonomous undersea vehicles. *IEEE Journal of Oceanic Engineering* 30: 109–139.
- Bartol IK, Krueger PS, Stewart WJ, et al (2009) Hydrodynamics of pulsed jetting in juvenile and adult brief squid *Loliguncula brevis*: Evidence of multiple jet 'modes' and their implications for propulsive efficiency. *Journal of Experimental Biology* 212: 1889–1903.
- Boxerbaum AS, Shaw KM, Chiel HJ et al. (2012) Continuous wave peristaltic motion in a robot. *The International Journal of Robotics Research* 31: 302–318.
- Calisti M, Giorelli M, Levy G et al. (2011) An octopus-bioinspired solution to movement and manipulation for soft robots. *Bioinspiration & Biomimetics* 6: 1–10.
- Choi H, Hanai A, Choi S et al. (2003) Development of an underwater robot, odin-iii. In: *Proceedings 2003 IEEE/RSJ International Conference on Intelligent Robots and Systems (IROS 2003)*, volume 1, Las Vegas, NV, 27–31 October 2003, pp. 836–841.
- Cianchetti M, Arienti A, Follador M et al. (2011) Design concept and validation of a robotic arm inspired by the octopus. *Materials Science and Engineering C* 31: 1230–1239.
- Colgate JE and Lynch KM (2004) Mechanics and control of swimming: A review. *IEEE Journal of Oceanic Engineering* 29: 660–673.
- Conte J, Modarres-Sadeghi Y, Watts M et al. (2010) A fast-starting robotic fish that accelerates at 40 ms^{-2} . *Bioinspiration & Biomimetics* 5(3): 035004.
- Eaton JW (2002) *GNU Octave Manual*. Bristol, UK: Network Theory Limited.
- Elvander J and Hawkes G (2012) Rovs and auvs in support of marine renewable technologies. In: *MTS/IEEE Oceans 2012*, Hampton Roads, VA, 14–19 October 2012, pp. 1–6.
- Giorelli M, Giorgio-Serchi F and Laschi C (2013) Forward speed control of a pulsed-jet soft-bodied underwater vehicle. In: *MTS-IEEE OCEANS*, San Diego, CA, USA, 23–27 September 2013, pp. 1–5.
- Giorgio-Serchi F, Arienti A, Baldoli I et al. (2013a) An elastic pulsed-jet thruster for soft unmanned underwater vehicles. In: *IEEE International Conference on Robotics and Automation*, Karlsruhe, Germany, 6–10 May 2013, pp. 5103–5110.
- Giorgio-Serchi F, Arienti A and Laschi C (2013b) Biomimetic vortex propulsion: Toward the new paradigm of soft unmanned underwater vehicles. *IEEE/ASME Transaction on Mechatronics* 18: 484–493.
- Giorgio-Serchi F, Arienti A and Laschi C (2013c) A soft unmanned underwater vehicle with augmented thrust capability. In: *MTS-IEEE OCEANS*, San Diego, CA, USA, 23–27 September 2013, pp. 1–5.
- Giorgio-Serchi F, Renda F, Calisti M et al. (2015) Thrust depletion at high pulsation frequencies in underactuated, soft-bodied, pulsed-jet vehicles. In: *OCEANS 2015 - Genova*, Genoa, Italy, 18–21 May 2015, pp. 1–6.
- Gosline JM and DeMont ME (1985) Jet-propelled swimming squids. *Scientific American* 252: 96–103.
- Guo S, Lin X, Tanaka K et al. (2010) Modeling of water-jet propeller for underwater vehicles. In: *IEEE International Conference on Automation and Logistics*, Hong Kong and Macau, 16–20 August 2010 pp. 92–97.
- Hover FS, Eustice RM, Kim A et al. (2012) Advanced perception, navigation and planning for autonomous in-water ship hull inspection. *The International Journal of Robotics Research* 31: 1445–1464.
- Johnson W, Soden PD and Trueman ER (1972) A study in jet propulsion: An analysis of the motion of the squid, *Loligo Vulgaris*. *Journal of Experimental Biology* 56: 155–165.
- Kazakidi A, Tsakiris DP, Angelidis D et al. (2015) Cfd study of aquatic thrust generation by an octopus-like arm under intense prescribed deformations. *Computers and Fluids* 115: 54–65.
- Kim S, Laschi C and Trimmer BA (2013) Soft robotics: A bioinspired evolution in robotics. *Trends In Biotechnology* 31: 287–294.
- Krieg M and Mohseni K (2008) Thrust characterization of a bio-inspired vortex ring generator for locomotion of underwater robots. *IEEE Journal of Ocean Engineering* 33: 123–132.
- Krieg M and Mohseni K (2010) Dynamic modeling and control of biologically inspired vortex ring thrusters for underwater robot locomotion. *IEEE Transactions on Robotics* 26: 542–554.
- Krieg M and Mohseni K (2013) Modeling circulation, impulse and kinetic energy of starting jets with non-zero radial velocity. *Journal of Fluid Mechanics* 79: 488–526.
- Krueger PS and Gharib M (2003) The significance of vortex ring formation to the impulse and thrust of starting jet. *Physics of Fluid* 15: 1271–1281.
- Laschi C, Mazzolai B, Mattoli V et al. (2009) Design of a biomimetic robotic octopus arm. *Bioinspiration & Biomimetics* 4: 1–8.
- Licht S, Polidoro V, Flores M et al. (2004) Design and projected performance of a flapping foil auv. *IEEE Journal of Oceanic Engineering* 29: 786–794.
- Lin HT, Leisk G and Trimmer BA (2011) Goqbot: A caterpillar-inspired soft-bodied rolling robot. *Bioinspiration & Biomimetics* 6(2): 026007.
- Macgillivray PS, Anderson EJ, Wright GM et al. (1999) Structure and mechanics of the squid mantle. *Journal of Experimental Biology* 202: 683–695.
- Marchese AD, Onal CD and Rus D (2014) Autonomous soft robotic fish capable of escape maneuvers using fluidic elastomer actuators. *Soft Robotics* 1: 75–87.
- Mörtl A, Lawitzky M, Kucukyilmaz A et al. (2012) The role of roles: Physical cooperation between humans and robots. *The International Journal of Robotics Research* 31: 1656–1674.
- Moslemi AA and Krueger PS (2010) Propulsive efficiency of a biomimetic pulsed-jet underwater vehicle. *Bioinspiration & Biomimetics* 5: 1–14.
- Otake M, Kagami Y, Inaba M et al. (2002) Motion design of a starfish-shaped gel robots made of electroactive polymer gel. *Robotics and Autonomous Systems* 40: 185–191.
- Pelrine R, Kornbluh R, Pei Q et al. (2000) High-speed electrically actuated elastomers with strain greater than 100%. *Science* 287: 836–839.

- Prandtl L (1952) *Essentials of Fluid Dynamics*. New York: Hafner Publications.
- Renda F, Giorgio-Serchi F, Boyer F et al. (2015a) Locomotion and elastodynamics model of an underwater shell-like soft robot. In: *Robotics and Automation (ICRA), 2015 IEEE International Conference on*, Seattle, WA, USA, 26–30 May 2015, pp. 1158–1165.
- Renda F, Giorgio-Serchi F, Boyer F et al. (2015b) Modelling cephalopod-inspired pulsed-jet locomotion for underwater soft robots. *Bioinspiration & Biomimetics* 10(5): 055005.
- Renda F, Giorgio-Serchi F, Boyer F et al. (2015c) Structural dynamics of a pulsed-jet propulsion system for underwater soft robot. *International Journal of Advanced Robotics System* 12(68): 1–18.
- Ruiz LA, Whittlesey RW and Dabiri JO (2011) Vortex-enhanced propulsion. *Journal of Fluid Mechanics* 668: 5–32.
- Saimek S and Li PY (2004) Motion planning and control of a swimming machine. *International Journal of Robotics Research* 23: 27–53.
- Sfakiotakis M, Kazakidi A, Chatzidaki A et al. (2014) Multi-arm robotic swimming with octopus-inspired compliant web. In: *IEEE/RSJ International Conference on Intelligent Robots and Systems*, Chicago, IL, 14–18 September 2014, pp. 302–308.
- Singh H, Yoerger D and Bradley A (1997) Issues in auv design and deployment for oceanographic research. In: *Proceedings of the 1997 IEEE International Conference on Robotics and Automation*, Albuquerque, NM, 22–24 April 1997, pp. 1857–1862.
- Staaf DJ, Gilly WF and Denny MW (2014) Aperture effects in squid jet propulsion. *The Journal of Experimental Biology* 217: 1588–1600.
- Sugiyama Y and Hirai S (2006) Crawling and jumping by a deformable robot. *The International Journal of Robotics Research* 25: 603–620.
- Thompson JT and Kier WM (2006) Ontogeny of mantle musculature and implications for jet locomotion in oval squid, *Sepioteuthis lessoniana*. *The Journal of Experimental Biology* 209: 433–443.
- Trimmer B (2013) Soft robots. *Current Biology* 23: 639–641.
- Trivedi D, Rahn CD, Kier WM et al. (2008) Soft robotics: Biological inspiration, state of the art, and future research. *Applied Bionics and Biomechanics* 5: 99–117.
- Trueman ER and Packard A (1968) Motor performances of some cephalopods. *Journal of Experimental Biology* 49: 495–507.
- Vasilescu I, Detweiler C, Doniec M et al. (2010) Amour v: A hovering energy efficient underwater robot capable of dynamic payloads. *The International Journal of Robotics Research* 29: 547–570.
- Weymouth GD, Subramaniam V and Triantafyllou MS (2015) Ultra-fast escape maneuver of an octopus-inspired robot. *Bioinspiration & Biomimetics* 10: 016016.
- Weymouth GD and Triantafyllou MS (2012) Global vorticity shedding for a shrinking cylinder. *Journal of Fluid Mechanics* 702: 470–487.
- Weymouth GD and Triantafyllou MS (2013) Ultra-fast escape of a deformable jet-propelled body. *Journal of Fluid Mechanics* 721: 367–385.
- Woodman R, Winfield AFT, Harper C et al. (2012) Building safer robots: Safety driven control. *The International Journal of Robotics Research* 31: 1603–1626.
- Xin B, Xiaohui L, Zhaocun S et al. (2013) A vectored water jet propulsion method for autonomous underwater vehicles. *Ocean Engineering* 74: 133–140. Downloaded from ijr.sagepub.com at LOYOLA MARYMOUNT UNIV on January 30, 2016
- Xydas N and Kao I (1999) Modeling of contact mechanics and friction limit surfaces for soft fingers in robotics, with experimental results. *International Journal of Robotics Research* 18: 941–950.
- Yoerger DR, Jakuba M, Bradley AM et al. (2007) Techniques for deep sea near bottom survey using an autonomous underwater vehicle. *The International Journal of Robotics Research* 26: 41–54.
- Yu J, Ding R, Yang Q et al. (2011) On a bio-inspired amphibious robot capable of multimodal motion. *IEEE Transactions on Mechatronics* pp. 1–10.
- Yu J, Tan M, Wang S et al. (2004) Development of a biomimetic robotic fish and its control algorithm. *IEEE Transactions on Systems, Man and Cybernetics, Part B* 34: 1798–1810.
- Zheng C, Shatara S and Xiaobo T (2010) Modeling of biomimetic robotic fish propelled by an ionic polymer-metal composite caudal fin. *IEEE Transactions on Mechatronics* 15: 448–459.

6. Appendix

Reference values of the design and hydrodynamics parameters are reported here respectively for Prototype-1, Table 1, Prototype-2, Table 2, and Prototype-3, Table 3.

Table 1. Nomenclature: The parameters and the variables of the model for Prototype-1.

Symbol	Description	Value
Geometric parameters		
l	Crank length	13.0 mm
L	Robot length	160.0 mm
N	Number of sections	4
M	Number of cables per section	6
r_1	Radius of section 1	32.63 mm
(x_0, y_0)	Location of the fixed pulley	$(0, -1.2)$
γ_{N1}	Point of attachment of cable 1	0°
γ_{N2}	Point of attachment of cable 2	60°
γ_{N3}	Point of attachment of cable 3	120°
γ_{N4}	Point of attachment of cable 4	180°
γ_{N5}	Point of attachment of cable 5	210°
γ_{N6}	Point of attachment of cable 6	270°
ΔS_1	Axial extent of section 1	37.0 mm
A_{nz}	Nozzle exit area	706.9 mm ²
V_{max}	Maximum amount of fluid in the shell	330 mL
V_{min}	Minimum amount of fluid in the shell	200 mL
Dynamic parameters		
ρ_{rb}	Density of rubber material	1.07 g/cm ³
C_d	Drag coefficient	1.2
C_f	Flow loss coefficient	0.95
C_f	Flow loss coefficient	0.6
V_e	Coefficient of inflation speed	10 cm/s ²
M_{th}	Mass of the thruster	336 g
X_{AM}	Added mass of the thruster	102.7 g

^aCoordinate of the fixed pulley (in cm) with respect to the center of the shell.

Table 2. Nomenclature: The parameters and the variables of the model for Prototype-2.

Symbol	Description	Value
Geometric parameters		
l	Crank length	15.0 mm
L	Robot length	210.0 mm
N	Number of sections	1
M	Number of cables per section	4
r_1	Radius of section 1	40.0 mm
(x_O, y_O)	Location of the fixed pulley	(0, 2.0)
γ_{N1}	Point of attachment of cable 1	20°
γ_{N2}	Point of attachment of cable 2	160°
γ_{N3}	Point of attachment of cable 3	200°
γ_{N4}	Point of attachment of cable 4	340°
ΔS_1	Axial extent of section 1	40.0 mm
A_{nz}	Nozzle exit area	803.8 mm ²
V_{max}	Maximum amount of fluid in the shell	530 mL
V_{min}	Minimum amount of fluid in the shell	430 mL
Dynamic parameters		
ρ_{rb}	Density of rubber material	1.07 g/cm ³
C_d	Drag coefficient	1.2
C_f	Flow loss coefficient	0.95
C_f'	Flow loss coefficient	0.6
V_e	Coefficient of inflation speed	10 cm/s ²
M_{th}	Mass of the thruster	550 g
X_{AM}	Added mass of the thruster	146.0 g

^aCoordinate of the fixed pulley (in cm) with respect to the center of the shell.

Table 3. Nomenclature: The parameters and the variables of the model for Prototype-3.

Symbol	Description	Value
Geometric parameters		
l	Crank length	13.0 mm
L	Robot length	160.0 mm
N	Number of sections	4
M	Number of cables per section	4
r_1	Radius of section 1	40.0 mm
r_2	Axial extent of section 2	33.42 mm
r_3	Axial extent of section 3	36.6 mm
r_4	Axial extent of section 4	31.0 mm
(x_O, y_O)	Location of the fixed pulley	(0, 3.6)
γ_{N1}	Point of attachment of cable 1	0°
γ_{N2}	Location of the fixed spot	60°
γ_{N3}	Location of the fixed spot	120°
γ_{N4}	Point of attachment of cable 2	180°
γ_{N5}	Point of attachment of cable 3	210°
γ_{N6}	Point of attachment of cable 4	270°
γ_{N7}	Point of attachment of cable 5	330°
ΔS_1	Axial extent of section 1	37.0 mm
ΔS_2	Axial extent of section 1	23.0 mm
ΔS_3	Axial extent of section 1	23.0 mm
ΔS_4	Axial extent of section 1	37.0 mm
A_{nz}	Nozzle exit area	706.9 mm ²
V_{max}	Maximum amount of fluid in the shell	330 mL
V_{min}	Minimum amount of fluid in the shell	200 mL
Dynamic parameters		
ρ_{rb}	Density of rubber material	1.07 g/cm ³
C_d	Drag coefficient	1.2
C_f	Flow loss coefficient	0.95
C_f'	Flow loss coefficient	0.6
V_e	Coefficient of inflation speed	10 cm/s ²
M_{th}	Mass of the thruster	336 g
X_{AM}	Added mass of the thruster	102.7 g

^a Coordinate of the fixed pulley (in cm) with respect to the center of the shell.

^b Shell points which are not affected by cable contraction, see Figure 8.